BBA - Molecular Basis of Disease 1870 (2024) 167193

Contents lists available at ScienceDirect

BBA - Molecular Basis of Disease

journal homepage: www.elsevier.com/locate/bbadis

# The IRE1α-XBP1 arm of the unfolded protein response is a host factor activated in SARS-CoV-2 infection

Jose Javier Fernández [a,b], Arturo Marín [b,c], Romel Rosales [b,c], Rebekah Penrice-Randal [d], Petra Mlcochova [e], Yolanda Alvarez [a,f], Fernando Villalón-Letelier [b], Soner Yildiz [b,c], Enrique Pérez [a,o], Raveen Rathnasinghe [b,c,g], Anastasija Cupic [b,c,g], Thomas Kehrer [b,c,g], Melissa B. Uccellini [b,c], Sara Alonso [a], Fernando Martínez [a], Briana Lynn McGovern [b], Jordan J. Clark [d,l], Parul Sharma [d], Yolanda Bayón [a,f], Andrés Alonso [a], Randy A. Albrecht [b,c], Kris M. White [b,c], Michael Schotsaert [b,c], Lisa Miorin [b,c], James P. Stewart [d,h], Julian A. Hiscox [d,i,j], Ravindra K. Gupta [e], Nerea Irigoyen [k], Adolfo García-Sastre [b,c,l,m,n,*], Mariano Sánchez Crespo [a,**], Nieves Fernández [a,f]

[a] *Unidad de Excelencia Instituto de Biomedicina y Genética Molecular, CSIC-Universidad de Valladolid, 47003 Valladolid, Spain*
[b] *Department of Microbiology, Icahn School of Medicine at Mount Sinai, New York, NY 10029, USA*
[c] *Global Health and Emerging Pathogens Institute, Icahn School of Medicine at Mount Sinai, New York, NY 10029, USA*
[d] *Department of Infection Biology and Microbiomes, Institute of Infection, Veterinary and Ecological Sciences, University of Liverpool, Liverpool, UK*
[e] *Cambridge Institute of Therapeutic Immunology & Infectious Disease (CITIID), Department of Medicine, University of Cambridge, Cambridge, UK*
[f] *Departamento de Bioquímica, Biología Molecular y Fisiología, Universidad de Valladolid, 47003 Valladolid, Spain*
[g] *Graduate School of Biomedical Sciences, Icahn School of Medicine at Mount Sinai, New York, NY 10029, USA*
[h] *Department of Infectious Diseases, University of Georgia, GA 30602, USA*
[i] *Infectious Diseases Horizontal Technology Centre (ID HTC), A*STAR, Singapore, Singapore*
[j] *Department of Preventive Veterinary Medicine, Northwest A&F University, Yangling, Shaanxi, China*
[k] *Division of Virology, Department of Pathology, University of Cambridge, Tennis Court Road, Cambridge, UK*
[l] *Department of Medicine, Division of Infectious Diseases, Icahn School of Medicine at Mount Sinai, New York, NY 10029, USA*
[m] *The Tisch Cancer Institute, Icahn School of Medicine at Mount Sinai, New York, NY 10029, USA*
[n] *Department of Pathology, Molecular and Cell-Based Medicine, Icahn School of Medicine at Mount Sinai, New York, NY 10029, USA*
[o] *Departamento de Ciencias de la Salud, Universidad Europea Miguel de Cervantes (UEMC), 47012 Valladolid, Spain*

ARTICLE INFO

*Keywords:*
COVID-19
Cytokines
Fluvoxamine
Pneumonia
TLR
Transcription factors
Unfolded protein response
Viral sepsis
Variants of concern

ABSTRACT

SARS-CoV-2 infection can cause severe pneumonia, wherein exacerbated inflammation plays a major role. This is reminiscent of the process commonly termed cytokine storm, a condition dependent on a disproportionated production of cytokines. This state involves the activation of the innate immune response by viral patterns and coincides with the biosynthesis of the biomass required for viral replication, which may overwhelm the capacity of the endoplasmic reticulum and drive the unfolded protein response (UPR). The UPR is a signal transduction pathway composed of three branches that is initiated by a set of sensors: inositol-requiring protein 1 (IRE1), protein kinase RNA-like ER kinase (PERK), and activating transcription factor 6 (ATF6). These sensors control adaptive processes, including the transcriptional regulation of proinflammatory cytokines. Based on this background, the role of the UPR in SARS-CoV-2 replication and the ensuing inflammatory response was investigated using *in vivo* and *in vitro* models of infection. Mice and Syrian hamsters infected with SARS-CoV-2 showed a sole activation of the Ire1α-Xbp1 arm of the UPR associated with a robust production of proinflammatory cytokines. Human lung epithelial cells showed the dependence of viral replication on the expression of UPR-target proteins branching on the IRE1α-XBP1 arm and to a lower extent on the PERK route. Likewise, activation of the IRE1α-XBP1 branch by Spike (S) proteins from different variants of concern was a uniform finding. These results show

* Correspondence to: A. García-Sastre, Department of Microbiology, Icahn School of Medicine at Mount Sinai, New York, NY 10029, USA
** Corresponding author at: Instituto de Biomedicina y Genética Molecular, C/Sanz y Forés 3, 47003 Valladolid, Spain.
*E-mail addresses:* adolfo.garcia-sastre@mssm.edu (A. García-Sastre), sanchezcrespomariano@gmail.com (M.S. Crespo).
[1] *Current affiliations:* Department of Microbiology and the Center for Vaccine Research and Pandemic, Icahn School of Medicine at Mount Sinai, New York, USA

https://doi.org/10.1016/j.bbadis.2024.167193
Received 9 September 2023; Received in revised form 30 March 2024; Accepted 16 April 2024
Available online 20 April 2024

that the IRE1α-XBP1 system enhances viral replication and cytokine expression and may represent a potential therapeutic target in SARS-CoV-2 severe pneumonia.

**Abbreviations**

| | |
|---|---|
| ACE2 | angiotensin converting enzyme 2 receptor |
| ATF6 | activating transcription factor 6 |
| BSL | biosafety level |
| CHOP | C/EBP homologous protein |
| CS | cytokine storm |
| DEGs | differentially expressed genes |
| dpi | days post-infection |
| dsRNA | double-strand RNA |
| ER | endoplasmic reticulum |
| FBS | fetal bovine serum |
| FDR | false discovery rate |
| GADD34 | growth arrest and DNA damage-inducible protein |
| GO | gene ontology |
| H&E | hematoxylin and eosin |
| hpi | hour post-infection |
| hpt | hours post-transfection |
| HRP | horseradish peroxidase |
| IFN | interferon |
| i.p. | intraperitoneal |
| IRE1α | inositol-requiring enzyme 1α |
| IRF | IFN regulatory factor |
| MA-SARS-CoV-2 | mouse-adapted SARS-CoV-2 |
| MOI | multiplicity of infection |
| PAMPs | pathogen-associated molecular patterns |
| pDC | plasmacytoid dendritic cells |
| PERK | PKR-like ER kinase |
| PFU | plaque-forming unit |
| RIDD | regulated IRE1-dependent mRNA decay |
| S protein | spike protein |
| s.c. | subcutaneous |
| SIR1 | SIGMAR1 chaperon |
| SSRI | selective serotonin reuptake inhibitor |
| ssRNA | single-strand RNA |
| *sXBP1* | spliced form of *XBP1* |
| STAT | signal transducer and activator of transcription |
| TMPRS2 | transmembrane serine protease 2 |
| TLR | Toll-like receptors |
| $TCID_{50}$ | 50 % tissue culture infectious dose |
| UPR | unfolded protein response |
| *uXBP1* | unspliced XBP1 |
| VOCs | variants of concern of S protein |
| WT | wild type |
| XBP1 | X-box binding protein 1 |

## 1. Introduction

Coronaviruses are enveloped, positive-sense RNA viruses with a single-stranded genome, the replication of which takes place in close association with intracellular membrane structures mainly provided by the endoplasmic reticulum (ER) [1]. The use of the host translational machinery in the replication cycle overloads many cellular functions, including the capacity of the ER to fold, assemble, and secrete proteins. The unfolded protein response (UPR) is an evolutionarily conserved adaptive mechanism triggered when misfolded proteins accumulate within the lumen of the ER. The global UPR activation drives a reduction of protein synthesis and increases the folding capacity because of the overproduction of chaperones and glycosylases that restore ER homeostasis. If this compensatory mechanism fails and ER stress persists, UPR-mediated cell death and inflammatory responses will ensue [2,3].

The UPR controls different signaling pathways arranged in three different arms. The sensors involved in these pathways are the PKR-like ER kinase (PERK), the activating transcription factor 6 (ATF6), and the inositol-requiring enzyme 1α (IRE1α). IRE1α is an ER transmembrane kinase that transactivates a C-terminal ribonuclease activity after *trans*-autophosphorylation. This drives the cleavage of an intron in the mRNA of X-box binding protein 1 (XBP1) and the expression of a functional transcription factor termed spliced XBP1 (sXBP1) [4]. Of note, the IRE1α-XBP1 arm of the UPR is also activated by the encounter of pathogen-associated molecular patterns (PAMPs) with Toll-like receptors (TLRs) and contributes to enhance the production of proinflammatory cytokines [5]. Based on these notions, we posited that the UPR might contribute to the pathogenesis of the hyperinflammatory response dubbed cytokine storm (CS)/viral sepsis associated with severe forms of COVID-19 disease.

Current therapies to counter CS have been dexamethasone and tocilizumab, an anti-human interleukin 6 (IL-6) receptor monoclonal antibody [6,7]. Studies directed to repurpose the use of available drugs for COVID-19 illness showed that fluvoxamine, a selective serotonin reuptake inhibitor (SSRI), prevented hospitalization and eased outpatient management in clinical studies [8,9]. The agonist effect of fluvoxamine on the ER chaperone SIGMAR1 (SIR1) was proposed as the purported mechanism of action of this drug. Likewise, SARS-CoV-2 non-structural protein 6 (nsp6) was found to interact with SIR1 [10,11], and the interference of fluvoxamine with this process explains why several SIR1 ligands have been explored as therapeutic tools in COVID-19 [12–14].

The purpose of this study was to analyze the occurrence of UPR activation during SARS-CoV-2 infection in mouse and hamster models and its potential association with viral replication. The antiviral and anti-inflammatory effects of fluvoxamine were also studied, as well as the mechanism whereby the viral spike (S) protein could induce UPR in the context of both viral infection and overexpression of different variants of concern (VOC) of S protein. The major finding of this investigation was the evidence of UPR activation during SARS-CoV-2 infection. Viral replication in human epithelial cells was found to be dependent on the activity of the IRE1α-XBP1 arm of the UPR. Fluvoxamine decreased the levels of peripheral blood cytokines in mice infected with a mouse-adapted SARS-CoV-2 (MA-SARS-CoV-2), but it did not show any significant effect on viral replication.

## 2. Materials and methods

### 2.1. Animal models of SARS-CoV-2 infection

Hemizygous 6-week-old female K18-hACE2 mice on the C57BL/6J background from the Jackson Laboratory (RRID:IMSR_JAX:034860) were compared to age and sex-matched wild type (WT) C57BL/6 J (RRID:IMSR_JAX:000664) and WT BALB/c (RRID:IMSR_JAX:000651) mice. Golden Syrian hamsters 8-week-old female (strain HsdHan®: AURA, Envigo). 129S1/SvImJ mice (RRID:IMSR_JAX:002448, Jackson Laboratory) were used for MA-SARS-CoV-2 infection and treatment with

subcutaneous fluvoxamine. All animal studies were performed in animal BSL3 facility at the Icahn School of Medicine in Mount Sinai Hospital, New York City. Animal studies were approved by the Institutional Animal Care and Use Committee (IACUC) of Icahn School of Medicine at Mount Sinai (ISMMS).

### 2.2. Cells and viruses

A549-ACE2 recombinant cells [15] and A549-ACE2/TMPRSS2 [16] were kind gifts from the referred laboratories. Vero E6 cells and HEK-293 T cells (ATCC) were maintained in DMEM supplemented with 10 % fetal bovine serum (FBS), 1 % non-essential amino acids, and penicillin/streptomycin at 37 °C and 5 % $CO_2$ atmosphere. All cell lines used in this study were regularly screened for mycoplasma contamination using MycoStrip™-Mycoplasma Detection Kit (InvivoGen). The following virus strains were used SARS-CoV-2, isolate USA-WA1/2020 (BEI Resources NR-52281) termed as WA1/2020, lineage B SARS-CoV-2/human/Liverpool/REMRQ0001/2020, α variant (B.1.1.7; SARS-CoV-2 England/ATACCC 174/2020) [17], and lineages B.1.1.617.2 (δ, GISAID: EPI_ISL_1731019) and B.1.1.529 (omicron UK isolate) [18,19]. MA-SARS-CoV-2 was utilized for *in vivo* experiments as reported [20]. Viruses were used under BSL3 containment in accordance with the biosafety protocols developed by the ISMMS and University of Cambridge and were grown in Vero-TMPRSS2 cells for 4–6 days. The supernatant was clarified by centrifugation at 4,000 *g* for 5 min and aliquots were frozen at −80 °C for long term use. Expanded viral stocks were sequence-verified and tittered on Vero-TMPRSS2 cells before use in all assays.

### 2.3. SARS-CoV-2 infection in mice

Mice were housed in a BSL2 facility for intranasal instillation of non-replicating adenoviral vectors before being transferred to a BSL3 facility for challenge with SARS-CoV-2. Mice were housed under specific pathogen-free conditions in individually ventilated cages and fed irradiated food and filtered water. Mice were infected with $1 \times 10^4$ PFU. Viral seed stocks for non-replicating E1/E3 deleted viral vectors based on human adenovirus type-5 HAdV-C5, referred to as Ad-Empty without an antigen or as Ad-hACE2 when expressing the human ACE2 receptor under the control of a CMV promoter were obtained from Iowa Viral Vector Core Facility. For *in vivo* delivery of Ad vectors to the lung, mice were anesthetized by i.p. injection of ketamine and xylazine. Ad-Empty at $2.5 \times 10^8$ PFU or Ad-hACE2 at a dose of $2.5 \times 10^8$ PFU were instilled intranasally in a final volume of 50 μL sterile PBS. Untreated control mice received the same volume of PBS. Mice were transferred to the BSL3 facility on day 3 post-Ad for subsequent challenge with SARS-CoV-2 virus on day 5. For SARS-CoV-2 challenge, mice were anesthetized as aforementioned and inoculated with $1 \times 10^4$ PFU in 50 μL of PBS *via* the intranasal route. Mice were sacrificed on day 2 and day 5 post-infection by i.p. injection of pentobarbital. Lungs were homogenized in 1 mL PBS using ceramic beads.

### 2.4. SARS-CoV-2 infection of golden Syrian hamsters

Experiments were conducted in 8-week-old female golden Syrian hamsters of approximately 120 g body weight. Hamsters were housed in ventilated cages with free access to food and water and environmental enrichment. Cages were situated in a BSL3 vivarium with a light-cycle of 14 h on, 10 h off. Experimental protocols were approved by the IACUC at ISMMS (protocol number: IACUC-2017-0330). Hamsters were intranasally mock-infected ($n = 8$) or infected with $5 \times 10^5$ PFU of rSARS-CoV-2 WT in a 100 μL total inoculum. Ketamine (100 mg/kg)/xylazine (5 mg/kg) was used to anesthetize the animals prior to infection. After infection, animals were monitored daily for morbidity and mortality up to 15-day post-infection (dpi). Necropsies were performed at 2, 4, 6, and 15 dpi. Animals were anesthetized with 200 μL ketamine/xylazine and terminally bleed. The top right lobe of the lung was harvested and homogenized in Trizol. Total RNA was isolated with the RiboPure Kit (ThermoFisher) as per the manufacturer's instructions. The bottom right lobe of the lung was homogenized in PBS and mixed at a 1:1 *v*/v ratio with RIPA (ThermoFisher) buffer supplemented with 1 % SDS, cOmplete protease inhibitor mixture (Roche), and Halt phosphatase inhibitor cocktail (ThermoFisher) before boiling for virus inactivation. Subsequently, samples were subjected to sonication before lysates were cleared by centrifugation. Proteins were quantified using the Pierce BCA Protein Assay.

### 2.5. Whole lung RNA and protein extraction

A portion of about 25 % of lung tissue was homogenized in Trizol, and RNA extracted using Direct-zol RNA Miniprep Plus kit (Zymo Research). The remaining lung tissue was used for protein extraction and homogenized in PBS with silica glass beads. The supernatant was mixed at a 1:1 *v*/v ratio with RIPA for 15 min in the BSL3 facilities prior to UV inactivation and centrifuged to eliminate the debris.

### 2.6. XBP1 splicing assay

This was carried out by RT-PCRs using primers outside the spliced region. The PCR conditions were 5 min at 95 °C (hot start), 45 cycles of denaturation at 95 °C for 15 s, annealing at 60 °C for 20 s, and elongation at 72 °C for 1 min. Final extension was carried out at 72 °C for 5 min. Gel electrophoresis was carried out in 3 % agarose, and *sXBP1* and *uXBP1* bands were visualized by GelRed® staining and quantified using GelDoc Go Image System. For Syrian hamster, PCR product *uXBP1* (XM_040746756.1) was digested with *Pst*I for 24 h at 37 °C, following the manufacturer's instructions.

### 2.7. qRT-PCR

RNA was reverse transcribed using maxima reverse transcriptase and oligo-dT18 (ThermoFisher Scientific). Quantitative RT-PCR was performed in cDNA using Light-Cycler 480 SYBR Green I Master Mix in a LightCycler 480 II. TaqMan probes (ThermoFisher Scientific) were used for the assay of *Hspa5* (Cg01333324_g1), *Ddit3*/Chop (Cg04519311_g1), *Atf4* (Cg04423842_g1), and *Actb* (Cg04424027_gH) in Syrian hamster, and *Herpud1* (Mm00445600_m1), *Edem1* (Mm00551797_m1), *Pdia3* (Mm004333130_m1), and *Actb* (Mm02619580_g1) in mice. Other sets of primers are shown in Table S1.

### 2.8. Western blot

Protein extract concentration was quantified using the Pierce BCA Protein Assay (ThermoFisher Scientific). 10 μg of protein extracts were resolved in 10 % Mini-PROTEAN® TGX Stain-Free™ Protein Gels (Bio-Rad), then transferred to nitrocellulose membranes. The lysates were used for Western blotting to determine the protein expression of CHOP, GADD34, XBP1, HERPUD1, and viral protein S. Briefly, membranes were incubated with rabbit mAb anti-sXBP1 (RRID:AB_2891025), mouse mAb anti-CHOP (RRID:AB_2089254), rabbit mAb β-actin (RRID: AB_1903890), and rabbit mAb anti-HRP conjugated (RRID: AB_1903890) from Cell Signaling. Mouse mAb anti-GADD34 (RRID: AB_296678), rabbit mAb anti-HERPUD1 (RRID:AB_2857374), and rabbit anti-SARS-CoV-2 viral glycoprotein Spike (S) (RRID:AB_2847845) from abcam were diluted at 1:1000. The HRP-conjugated anti-mouse IgG antibody (RRID:AB_378497) and the HRP-conjugated anti-rabbit IgG antibody (RRID:AB_378894) from GeneTex were used to detect the primaries antibodies at 1:10000. HRP was detected using Clarity™ Western ECL Substrate (Bio-Rad). Each protein band was quantified by ImageJ free software and normalized to GAPDH or β-actin levels. IRDye 800CW donkey anti-rabbit IgG (H + L) (RRID:AB_621848), IRDye 680RD goat anti-mouse IgG (H + L) (RRID:AB_10956588), and IRDye

680RD goat anti-mouse IgM (μ chain specific) (RRID:AB_2814921) were from Li-COR Biosciences.

### 2.9. Bioinformatics analysis in K18-hACE2 mice

Trimming of Illumina paired-end sequencing reads derived from K18-hACE2 mice infected with the UK strain of SARS-CoV-2 was performed as described previously [21]. Briefly, the raw fastq files (2 × 150 bp) generated by an Illumina® NovaSeq 6000 were trimmed to remove Illumina adapter sequences using Cutadapt v1.2. The option "−O 3" was set, so that the 3′ end of any reads which matched the adapter sequence with >3 bp was trimmed off. The reads were further trimmed to remove low quality bases, using Sickle v1.200 with a minimum window quality score of 20. After trimming, reads shorter than 10 bp were removed. The mouse genome (GRCm39.primary_assembly.genome.fa) and corresponding annotation (gencode.vM27.primary_assembly.annotation.gtf) was indexed using STAR (v.2.7.10b) [22]. Trimmed sequencing reads were aligned to the index before taking SortedByCoordinate bam files into featureCounts (v.2.0.1) (sourceforge.net). FeatureCounts output for mouse analysis were imported into R using DESeq2 [23] and EdgeR [24]. Data resulting from applying these methods for the calculation of differential expression were filtered using the thresholds Log2FoldChange ≥ 1 and *p*-value <0.05. GO enrichment pathways derived from *Mus musculus* were identified. CAMERA (Correlation Adjusted Mean Rank) method [25] was employed implemented by the R package "Enrichmentbrowser" v2.2.2. Then, we selected differential biological processes according to ER function with an FDR < 0.05, represented as bubble color. The number of genes within the GO pathway was represented as bubble size using Prism software.

### 2.10. Bioinformatics analysis in Syrian hamsters

For the analysis in Syrian hamsters, the reads from the Illumina paired-end sequencing were processed with the Trimmomatic v0.36 program (USADELLAB.org) to filter out low-quality reads and to trim the adapters. Then, a check of the Trimmomatic results was carried out using FastQC v0.11.9 (Babraham Bioinformatics) and MultiQC v1.11 (MultiQC). It was verified that the mean value of the Phred quality score for all the samples was greater than Q30 and that the rest of the parameters were within the normal values for RNA samples. The available assembled genomes of *Mesocricetus auratus* were studied to verify that their corresponding annotation files contained the genes of interest for the study. It was concluded that the best assembled and annotated genome for our purposes was that of the Baylor College of Medicine Human Genome Sequencing Center (RefSeq assembly accession GCF_017639785.1). With said reference genome and using the HISAT2 v2.2.1 program [26], the mapping of the cleaned reads was carried out. Using SAMtools v1.12 (GitHub.com) the SAM files produced in the mapping were transformed into ordered BAM files and indexed in a later step. To count the reads that map against each of the *Mesocricetus auratus* genes, it was necessary to make a small modification to the GTF annotation file. The original GTF file has no gene identifier for some gene id in the 9th column. Seeing that in the "product" field it was indicated that these entries were tRNA, and that they were not relevant for our research, it was decided to eliminate these entries to carry out the analysis. With the fixed GTF file, the mapping BAM files, and the featureCounts v2.0.1 program (Bioconductor), the count of the reads that map against each of the genes was carried out. When the table of counts was obtained, the differential expression analysis was carried out using the DESeq2 and EdgeR programs. Finally, volcano plots of the significant genes object of study were represented using the library EnhancedVolcano v1.14.0 of R v4.2.0 (Bioconductor). For further gene sets analysis, GO enrichment pathways derived from *Mus musculus* and *Rattus norvegicus* genome were identified instead of *Mesocricetus auratus* genome, which was not annotated. Thus, the CAMERA method was employed implemented by the R package "Enrichmentbrowser" v2.2.2 (Bioconductor). We selected differential biological processes according to ER function, viral process, inflammation, and cytokines with an FDR < 0.05, represented as bubble color. The number of genes within the GO pathway was represented as bubble size using Prism software. To compare the number of genes significantly enriched with data available from Calu-3 cells [27], the tables resulting from applying the EdgeR method for the calculation of differential expression in the Syrian hamster were filtered using the thresholds Log2FoldChange ≥ 1 and *p*-value <0.05. Likewise, the file star_top_table_Cov2_over_Mock_full.txt of the Calu-3 study was also filtered using Log2FoldChange ≥ 1 and p-value <0.05 thresholds. The gene lists resulting from the filtering were compared using the VennDiagram library of R to generate Venn diagrams.

### 2.11. Lung viral titers

129S1/SvImJ female mice 4-week-old specific pathogen-free were used. These mice were anesthetized with a mixture of ketamine/xylazine before each intranasal infection with MA-SARS-CoV-2 and compared to a group treated with 150 mg/kg fluvoxamine. On day 3 post-infection, animals were humanely euthanized. Weight data were transformed into body weight percentage. Lungs were harvested for viral titration and histopathology. The whole lung was homogenized and then frozen at −80 °C for viral titration *via* $TCID_{50}$. Briefly, infectious supernatants were collected at 48 hpi and frozen at −80 °C until later use. Infectious titers were quantified by limiting dilution titration using Vero TMPRS2 cells. Briefly, Vero-TMPRS2 cells were seeded in 96-well plates at 20,000 cells/well. Next day, SARS-CoV-2-containing supernatant was applied at serial 10-fold dilutions ranging from $10^{-1}$ to $10^{-8}$ and after 4 d, viral cytopathic effect was detected by staining cell monolayers with crystal violet.

### 2.12. Histopathology

Mice were euthanized with pentobarbital and death confirmed by exsanguination. After death, the trachea was exposed, and lungs inflated with 1.5 mL of 10 % formalin. Lungs were removed intact, trimmed carefully, and loaded into a tissue embedding cassette. The tissue was fixed overnight in 10 % formalin, transferred to PBS after 24 h and sent for processing and paraffin embedding at the Biorepository and Pathology Core at ISMMS. Paraffin-embedded lung tissue blocks for mouse lungs were cut into 5 μm sections, which were stained with H&E and analyzed by HistoWiz Inc. Digital light microscopic scans of whole lung processed were examined by an experienced veterinary pathologist. Hematoxylin and eosin (H&E)-stained sections from 129S1 mice were examined by implementing a semi quantitative, 5-point grading scheme (0 - within normal limits, 1 - mild, 2 - moderate, 3 - marked, 4 - severe), which considered four different histopathological parameters: 1) perivascular inflammation, 2) bronchial and bronchiolar epithelial degeneration or necrosis, 3) bronchial and bronchiolar inflammation, and 4) alveolar inflammation.

### 2.13. Analysis of peripheral blood cytokines

Cytokine levels in serum of mice infected with MA-SARS-CoV-2 were measured in inactivated samples. Sera were collected after centrifugation at 3000 *g* for 5 min, deactivated by UV, and stored at −80 °C. Cytokine analysis was performed at Eve Technologies using the Mouse Cytokine Array/Chemokine Array 44-Plex immunoassay.

### 2.14. Viral RNA and protein extraction in A549-ACE2 cells

A549-ACE2 cells were seeded at 1 × $10^6$ cells per well in BSL2 in DMEM supplemented with 10 % FBS, 1 % non-essential amino acids, and penicillin/streptomycin at 37 °C and 5 % $CO_2$ atmosphere. The day of the experiment, cells were transferred to BSL3, and media were replaced

by complete DMEM with 2 % FBS containing SARS-CoV-2 WA1/2020 at 0.1 and 1 MOI. Cells were harvested at 4, 8, 16, and 24 hpi using RIPA lysis and extraction buffer with protease inhibitor cocktail. RNA extracted from 1 × 10*6 A549-ACE2 cells were used for retro transcription (150–500 ng total RNA input). Quantitative PCR was run as described below. Then, viral RNA was calculated by quantification of *N* gene expression normalized to *GAPDH*.

### 2.15. siRNA knockdown of CHOP, GADD34, and XBP1

A549-ACE2 cells were transfected with 20 nM siRNA against human *DDIT3*/CHOP (J-004819-06-0002), human *GADD34* (J-004442-05-0002) and human *XBP1* (J-009552-07-0002), Dharmacon™. A negative control siGENOME non-targeting siRNA (D-001206-13-05, Dharmacon™) was used at the same concentrations of the siRNA described above. Gene knockdown was performed using $1 \times 10^6$ cells per well using Lipofectamine RNAiMAX Transfection Reagent (Invitrogen) following manufacturer's protocol for A549 cells. Tunicamycin 10 μM was used as a positive control of UPR activation for 6 h. After 24 h post-transfection (hpt), plates were transferred into the BSL3 facility, transfection media was removed, and cells were infected with SARS-CoV-2 at 1 MOI for 2 h, infectious media was removed and replaced to a new media and cells were harvested at 16 hpi for Western blot analysis and supernatants used for plaque assay.

### 2.16. Plaque assay

Plaque assays were performed using Vero E6 cells as previously described [28]. Briefly, Vero E6 cells seeded in 12-well plate format were infected with serial ten-fold dilutions of supernatants from A549-ACE2 cells used in siRNA experiments. Virus adsorption was carried out for 1 h using an inoculum of 200 μL and rocking the plates every 10–15 min. After 1 h, the inoculum was removed, and cells incubated with an overlay composed of MEM with 2 % FBS and 0.7 % Oxoid agar for 72 h at 37 °C with 5 % $CO_2$ atmosphere. The plates were subsequently fixed using 5 % formaldehyde and immuno-stained using an anti-SARS-CoV-N mAb. Plates were blocked (3 % skim-milk TBS with 0.1 % Tween20 for 1 h), stained for 90 min with anti-N antibody, and finally secondary-stained with anti-mouse-HRP (antibody diluted 1:5000 in 1 % skim-milk TBS with 0.1 % Tween20 for 45 min). Plates were incubated for 10 min with peroxidase substrate to reveal staining.

### 2.17. Plate-based cytometer image

Five thousand A549-ACE2 cells were seeded into 96-well plates in DMEM and incubated for 24 h at 37 °C in 5 % $CO_2$ atmosphere. Gene knockdown was performed using 20 nM siRNA using Lipofectamine RNAiMAX Transfection Reagent following manufacturer's protocol for A549 cells. After 24 h, plates were transferred into the BSL3 facility, and 0.1 or 0.2 MOI were added in 50 μL of DMEM supplemented with 2 % FBS. After 2 h, the inoculum was removed, and plates incubated for 24 and 48 h at 37 °C. After infection, supernatants were removed, and cells were fixed with 4 % formaldehyde for 24 h before being removed from the BSL3 facility. Cells were then immunostained for the viral N protein with DAPI counterstain. Infected cells and total cells were quantified using a Celigo (Nexcelcom) imaging cytometer. Infectivity was measured by the accumulation of viral N protein. The percentage of infection was quantified as (Infected cells/Total cells − Background) × 100. The DMSO control was then set to 100 % infection for analysis.

### 2.18. Plasmids and transfections

All SARS-CoV-2 S protein VOC plasmids (a kind gift of Dr. Thomas Peacock and Prof Wendy Barclay, Imperial College London) were human codon-optimised with the delta19 mutation (K1255*stop codon), which increases cell surface expression. To express the full-length protein, the stop codon was corrected by standard site-directed mutagenesis using the following primers (5′-GGCAGCTGCTGCAAGTTCGACGAGG and 5′-CCTCGTCGAACTTGCAGCAGC TGCC).

HEK-293 T cells were transiently transfected with full-length pcDNA3.1-SARS-CoV-2-S protein VOC plasmids, namely WT (D614G), β (B1.351), γ (P.1), δ (B1.617.2), and omicron (BA.1 and BA.2) using the liposome reagent TransIT®-LT1 (Mirus). Transfection mixtures containing plasmid DNA, serum-free medium, and liposomes were set up as recommended by the manufacturer and added dropwise to the tissue culture growth medium. Cells were harvested at 36 hpt.

### 2.19. A549-ACE2/TMPRSS2 VOC infection experiments

A549-ACE2/TMPRSS2 cells were seeded at $5 \times 10^5$ cells per well in DMEM supplemented with 10 % FBS, 1 % non-essential amino acids, and penicillin/streptomycin in a BSL2 containment laboratory. The day of the experiment, cells were transferred to a BSL3 containment laboratory and infected with SARS-CoV-2 WT, B.1.1.7 (α), δ, and omicron VOCs at 0.1 MOI 0.1. After the adsorption hour, media were replaced with complete DMEM supplemented with 10 % FBS. 10 μM KIRA8 was added to the DMEM-10 % FBS immediately after the virus adsorption period and maintained in the medium. Cells were harvested at 16 hpi using Laemmli's buffer for protein extraction and RNeasy kit (Qiagen) for RNA extraction. Viral RNA in SARS-CoV-2 infected cells was quantified by *N* gene expression normalized to *RPL19*. SARS-CoV-2 viral titers were assessed using a $TCID_{50}$ assay in Vero E6 cells. Supernatant derived from infected A549-ACE2/TMPRSS2 cells was subjected to 10-fold serial dilutions. At 72 hpi, cells were fixed and stained. Wells showing any sign of cytopathic effect were scored as positive.

### 2.20. Statistical analysis

All statistical analyses were performed using GraphPad Prism 9. Comparison between two groups was assessed using unpaired or paired (for matched comparisons) two-tailed Student's *t*-test. Multiple comparisons were evaluated by one-way ANOVA. Where applicable, error bars represent the mean ± standard error of the mean (SEM). *P*-values $<0.05$ were considered statistically significant. RNA data is shown as relative expression ($2^{-\Delta Ct}$ relative to *Actb*) or fold induction. sXBP1 was measured using the ratio sXBP1/XBP1$^T$(uXBP1 + sXBP1). $TCID_{50}$/mL were calculated using the method of Reed and Muench.

## 3. Results

### 3.1. SARS-CoV-2 infection induces UPR activation in K18-hACE2 mice

Unlike more recent variants, ancestral strains of SARS-CoV-2 do not infect wild-type laboratory mice [29], which makes it necessary the use of engineered mice for functional studies. The delivery of an adenovirus expressing the human ACE2 receptor (Ad-hACE2) or the use of the K18 transgenic hACE2 (K18-hACE2) mice are suitable models. While the Ad-hACE2 model causes a moderate ailment, infection is lethal in K18-hACE2 mice. In fact, Ad-hACE2 infection shows viral titers in lungs and nasal turbinates, while in K18-hACE2 mice viruses spread to other organs, *e.g.*, brain, spleen, and gut. This causes rapid weight loss and uniform lethality [21,30]. The induction of UPR-regulated genes was investigated in lungs of Ad-hACE2 transduced mice infected with an ancestral strain of SARS-CoV-2. Analysis of RNA extracted from homogenized lungs of C57BL/6 and BALB/c mice, transduced *in vivo* with Ad-hACE2 prior to infection with $1 \times 10^4$ plaque forming units (PFU) of the WA1/2020 strain of SARS-CoV-2 (Fig. S1 A), showed a similar pattern of *sXbp1* under all conditions of infection, *i.e.*, PBS, Ad-empty and Ad-hACE2, at 2 and 5 dpi, which indicates some degree of constitutive *XBP1* splicing (Fig. S1B and S1C). Lung expression of *Hspa5*, *Atf4*, and *Ddit3*, which encodes C/EBP homologous protein (Chop), did not show any change after infection, thus ruling out global activation of UPR

genes dependent on the Atf6 and Perk arms in C57BL/6 and BALB/c mice (Fig. S1D and S1E). Infection of K18-hACE2 mice with $1 \times 10^4$ PFU of ancestral SARS-CoV-2 strain WA1/2020 induced severe disease, including a strong induction of sXbp1 mRNA and protein at 2 dpi in comparison with animals at 5 dpi or uninfected mice (Fig. 1A-C). *Hspa5*, also called BiP or GRP78, which has been reported to behave as a pro-viral factor for SARS-CoV-2 [31,32], paralleled the pattern of *sXbp1* expression at 2 dpi. In contrast, the genes of the Perk arm, *Atf4* and *Ddit3* were not modified, nor was Chop protein (Fig. 1B and C). These data disclose a correlation between the early activation of the Ire1α-Xbp1 branch of the UPR and severe disease in the K18-hACE2 mouse model, as deemed from the presence of lung viral replication, weight loss, and lethality (Fig. 1D and F). To scrutinize the outcomes of the activation of the Ire1α-Xbp1 arm, transcriptomic analyses were performed of the RNA extracted from lungs harvested at 3 and 7 dpi from K18-hACE2 mice infected with $1 \times 10^4$ PFU of the SARS-CoV-2 lineage B strain. Principal component analyses showed a distinct separation of global gene expression profiles (Fig. 2A). Bioinformatic analysis of RNA-sequencing data confirmed higher levels of UPR-dependent genes at 3 dpi compared to 7 dpi (Fig. 2B). Moreover, the gene ontology (GO) analysis related to ER function showed ten pathways upregulated at 3 dpi and six pathways upregulated at 7 dpi, including biological processes related to *N*-linked glycosylation, chaperone-mediated functions, and ER stress-mediated UPR (Fig. 2C and D). It has been shown that the IRE1α-XBP1 branch contributes to the transcriptional activation of genes driving inflammation and immunosuppression in monocytes [33]. The analysis of differentially expressed genes (DEGs) showed a different pattern of cytokine induction at 3 and 7 dpi, particularly *Il6* increased at day 3, while *Il10* and *Il1r2*, which negatively regulates IL-1β signaling, increased at day 7 (Fig. 2E). These data suggest specific regulatory pathways involved at different times in the host inmune response and antiviral defense, as deemed from the pattern of cytokine expression during infection.

Based on the evidence that SARS-CoV-2 replication can stress the ER and activate different UPR-target genes, RT-PCR assays were conducted for confirmation in mice infected with SARS-CoV-2 strain WA1/2020. An increased expression of the canonical sXbp1-target gene *Dnajb9* but not *Sec61a1* was found (Fig. S2A). The expression of other UPR target genes such as *Herpud1, Edem1*, and *Pdia3* was not modified (Fig. S2B). The regulated IRE1-dependent mRNA decay (RIDD) is responsible for the direct degradation of a number of mRNAs since the IRE1α RNAse activity not only catalyzes the sequence-specific cleavage of 26 nucleotides of *Xbp1* mRNA, but also a small set of mRNAs sharing the common consensus sequence CUGCAG located in the stem-loop structure [34]. RIDD-dependent genes *Rpn1, Tapbp, Erp44, Hgsnat*, and *Bloc1s1* did not show any sign of activation at both $10^4$ and $10^5$ PFU of SARS-CoV-2

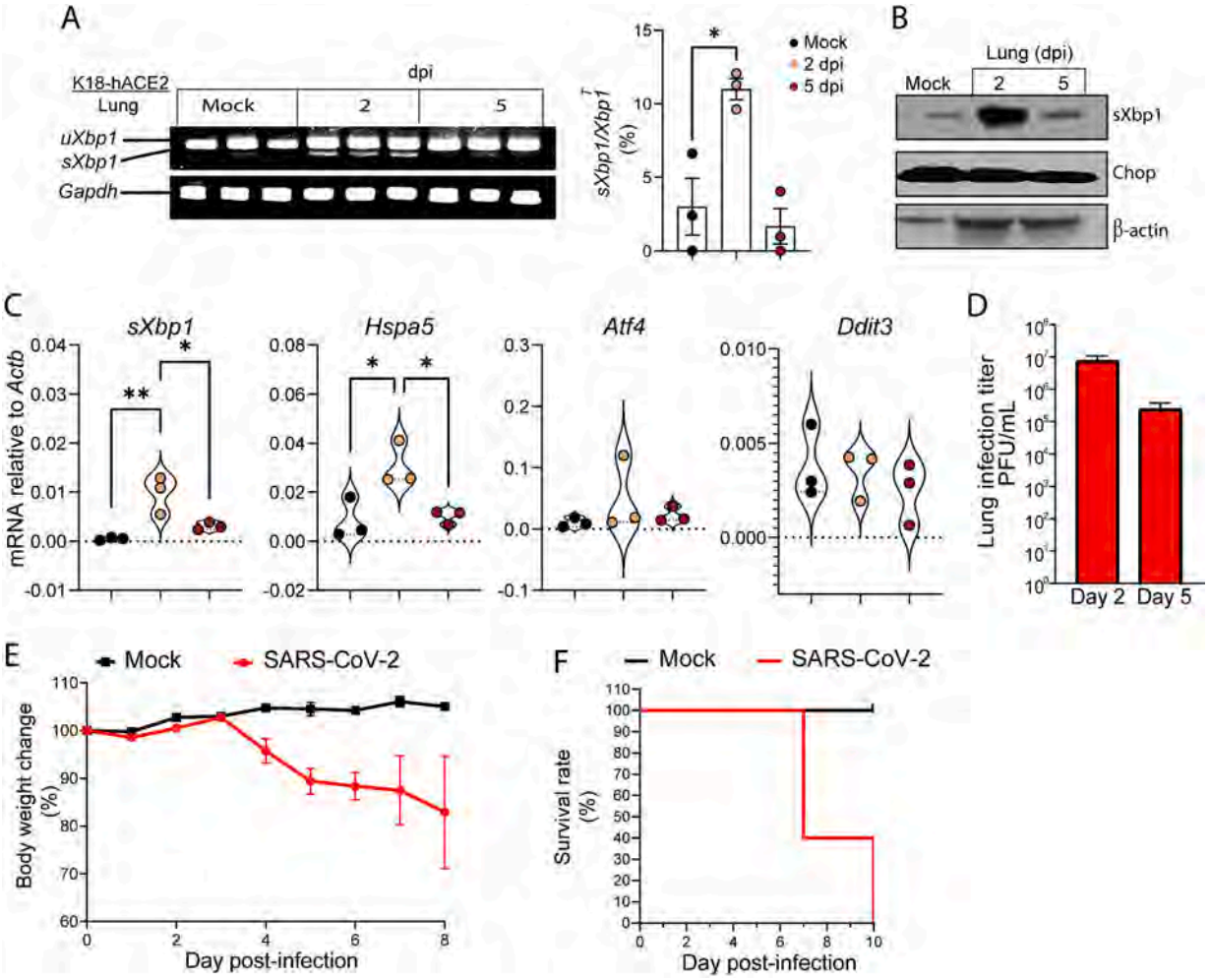


**Fig. 1.** SARS-CoV-2 activates the Ire1α-Xbp1 arm of the UPR in the lungs of K18-hACE2 mice after infection with $1 \times 10^4$ PFU of the ancestral SARS-CoV-2 strain WA1/2020. (A) Analysis of *Xbp1* by RT-PCR and resolution in agarose gel of the amplicons of three independent animals per condition (left panel) and quantification of *sXbp1*(right panel). (B) Western blot of sXbp1 and Chop in Mock and infected mice at 2 and 5 dpi. (C) Analysis of the mRNA of *sXbp1*, *Hspa5*, *Atf4*, and *Ddit3*. (D) Assay of viral titers measured by $TCID_{50}$ on days 2 and 5 in lung tissue. (E) Weight loss monitored in animals up to 10 days after infection. (F) Percentage of survival. Data are presented as mean ± SEM. $^*p < 0.05$, $^{**}p < 0.01$. Unpaired Student's *t*-test.

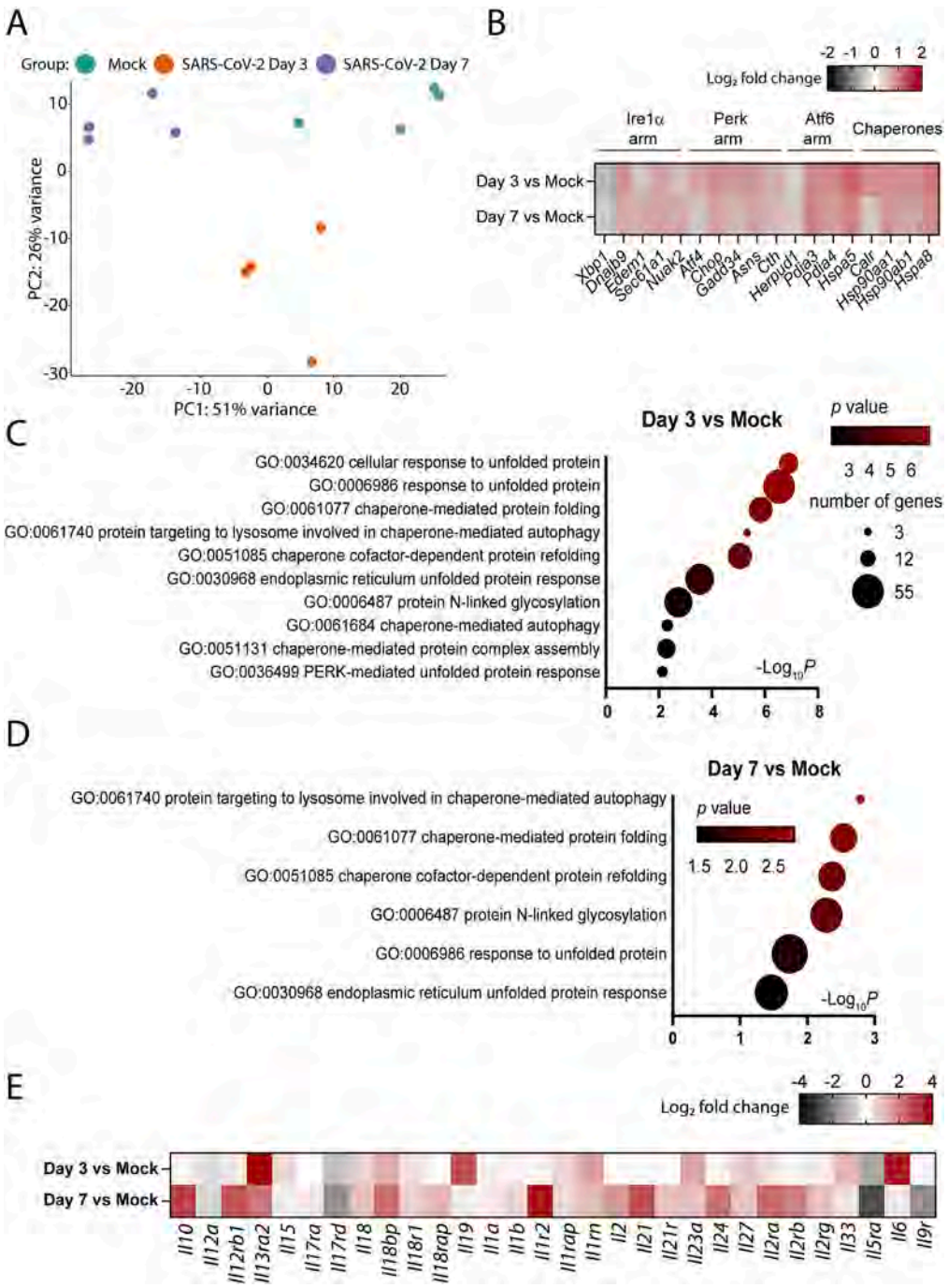


**Fig. 2.** Bioinformatic analysis of the lung tissue of K18-hACE2 mice during SARS-CoV-2 infection. (A) Principal component analysis showing distinct clustering of each group of animals. (B) Heat map of UPR genes comparing lung tissue in Mock mice with mice infected with $1 \times 10^4$ PFU of ancestral SARS-CoV-2 strain lineage B at 3 and 7 dpi. (C-D) GO enriched pathways analysis related to ER function at 3 and 7 dpi. Data are represented as bubble color with FDR < 0.05, and the number of genes within the GO pathway are represented as bubble size. (E) Heat map of cytokines comparing mock with 3 and 7 dpi. DEG analysis was carried out by DESeq2, and data are represented as $Log_2$ fold change.

WA1/2020 infection at 2 and 5 dpi (Fig. S2C and S2D). Moreover, RT-qPCR and bioinformatic analysis of RNA-seq data from mice infected with $1 \times 10^4$ PFU of the lineage B strain at 3 and 7 dpi did not show significant changes of expression of these genes (Fig. S2E). In summary, K18-hACE2 mice showed a strong but focused activation of some of the UPR pathways, as compared to a weaker activation in Ad-hACE2 infected mice.

### 3.2. *SARS-CoV-2 infection drives activation of the Ire1α-Xbp1 arm in the golden Syrian hamster model*

The clinical course of SARS-CoV-2 infection in the Syrian hamster model shows significant changes in temperature and weight loss by 3 dpi, and severe pneumonia and extrapulmonary damage around 5 dpi. Complete resolution occurs by day 14 [35,36]. This reproduces COVID-19 illness better than the K18-hACE2 mice and allows a protocol for sample collection consistent with the purported disease evolution. A systematic bioinformatic analysis addressed pathways related to ER

function in lung samples obtained from Syrian hamsters infected with 5 × $10^5$ PFU of rSARS-CoV-2 WT at 6 dpi. GO enriched pathway analysis showed upregulation of chaperone-mediated function and protein folding, *N*-linked and *O*-linked glycosylation, cellular stress responses, and UPR (Fig. 3A). The expression of UPR-target genes at 2, 4, and 6 dpi increased over time. This includes: *Xbp1*, *Hspa5*, *Hspa8*, *Nuak2*, *Calr, Pdia4, Tor1b, Tor3a, Sec61b, Hsp90ab1*, *Asns, Dnajc6* and *Dnajc22*. In contrast, *Atf4, Ddit3*/Chop, and *Gadd34* were not significantly upregulated at 6 dpi (Fig. 3B and C). Lung RNA analysis by RT-qPCR confirmed the bioinformatic analysis data. Accordingly, the mRNA expression of *Hspa5* was upregulated at 6 dpi, whereas *Atf4*, *Ddit3*, and *Gadd34* did not change significantly (Fig. S3A). To determine the presence of *Xbp1* splicing during infection in this model, RT-PCR assays were carried out using primers flanking the *Xbp1* gene sequence to amplify the unspliced (*uXbp1*, XM_040746756.1) and the spliced transcripts (*sXbp1*, XM_005067933.4) followed by resolution of the PCR products by agarose gel electrophoresis. Our first attempt did not show any significant change of expression between uninfected and infected Syrian hamsters at 2, 4, and 6 dpi (Fig. S3B). Then, we spanned both sequences to find out a restriction enzyme *Pst*I that cleaves the DNA at the recognition sequence 5′-CTGCA/G-3′, only present in the *uXbp1*. Although 24 h of incubation of the amplicons with PstI did not fully digest *uXbp1*, we found that this treatment, by driving fragmentation of *uXbp1*, allowed a better identification of *sXBP1*, mainly at 2 dpi (Fig. S3C). The confirmatory assay using primers flanking the spliced region of *Xbp1* showed that *sXbp1* increases at day 2, 4, and 6 in comparison with Mock (Fig. S3D). This was further corroborated at the protein level in lung tissue harvested at 6 dpi (Fig. S3E). Chop expression did not show significant differences in four infected animals as compared to Mock, while sXbp1 was upregulated (Fig. 3D and E). These findings reinforce the idea that SARS-CoV-2 infection promotes activation of the Ire1α-Xbp1 arm, while it mostly eludes the Perk/Atf4/Chop branch, consistent with the results observed in K18-hACE2 mice.

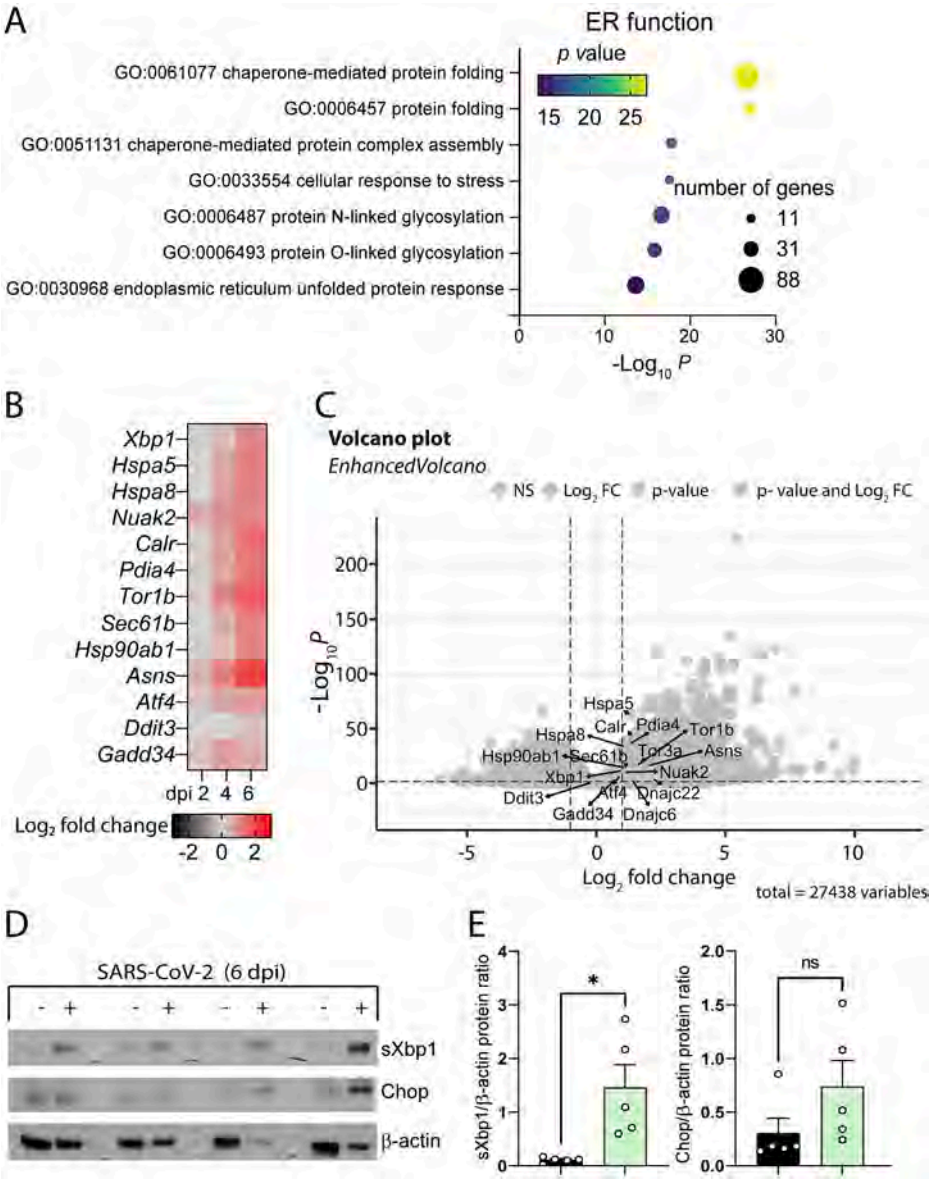


**Fig. 3.** SARS-CoV-2 infection drives activation of the Ire1α-Xbp1 arm of the UPR in the lungs of Syrian hamsters. (A) GO enriched pathways analysis and differential biological processes related to ER function at 6 dpi. (B) Heat map of UPR target genes comparing Mock with Syrian hamsters infected with 5 × $10^5$ PFU of rSARS-CoV-2 WT. Lungs were collected at 2, 4, and 6 dpi. (C) Volcano plot of UPR genes at 6 dpi. Significant genes are represented with a cut-point of 1 in $Log_2$ fold change and -$Log_{10}P$. The differential expression analysis shown was carried out using the DESeq2 program. The significant genes object of study are represented using the library EnhancedVolcano v1.14.0 of R v4.2.0 (Bioconductor). (D-E) Western blot analysis of sXbp1 and Chop proteins at 6 dpi and densitometric quantification.

### 3.3. Increased cytokine levels in golden Syrian hamsters infected with SARS-CoV-2

A bioinformatic analysis of RNA-seq data focusing on GO-enriched pathways related to global viral defense and inflammatory response mediated by TLRs was carried out in Syrian hamsters infected with $5 \times 10^5$ PFU of rSARS-CoV-2 WT at 6 dpi. Upregulation of nine GO pathways, *i.e.*, viral defense, response to virus, viral replication, and viral entry was observed (Fig. S4A), in agreement with what is expected during viral infection. In addition, GO inflammatory pathways were also activated during SARS-CoV-2 infection, including TLR2, TLR3, and TLR7 pathways (Fig. S4B). TLR2 locates at the cell surface, which suggests its involvement in the recognition of SARS-CoV-2 structural proteins, while TLR3 and TLR7 are endosomal receptors engaged in the recognition of double-strand RNA (dsRNA) and single-strand RNA (ssRNA), respectively. TLR signaling elicits canonical antiviral response involving interferon (IFN) and IFN regulatory factors (IRF) and signal transducer and activator of transcription (STAT) families, which drive expression of cytokines that limit viral spreading and elicit inflammation [37]. Analysis of DEGs at 2, 4, and 6 dpi showed an increase of *Irf1–9*, especially *Irf-7* (Fig. S4C). STAT family analysis also showed increased expression of *Stat1–2* but not the other STAT family components *Stat3–6* (Fig. S4D). IFN family analysis showed increased expression of *Ifnb1, Ifnl3, Isg15–20, Mx1*, and *Oas1–2*. However, *Ifnk* and the IFN receptors *Ifnar1–2* and *Ifngr1–2* decreased during infection (Fig. S4E). These results indicate that the evasion of SARS-CoV-2 of IFN responses may include the downregulation of IFN receptor expression [38]. In addition, twenty-nine different GO pathways related to signaling, regulation, and production of cytokines, including *Il1b, Il4, Il6, Il7, Il10, Il12, Il17*, *Tnf*, and chemokine related pathways were upregulated at 6 dpi (Fig. 4A). The analysis of cytokines showed increased levels along infection, with maximal expression at 6 dpi and, therefore, a potential chance for CS (Fig. 4B). Together, these results indicate that the SARS-CoV-2 infected Syrian hamsters show innate immune activation dependent on signaling routes driving viral defense and overproduction of cytokines.

### 3.4. Effect of fluvoxamine on viral replication and cytokine induction during MA-SARS-CoV-2 infection

ER stress can be relieved by the drug fluvoxamine, and several clinical studies reported the beneficial effect of this drug in COVID-19 sickness [9,39] and even proposed its use for the control of inflammation [40,41]. On this basis, the impact of fluvoxamine treatment in SARS-CoV-2 infection was addressed. 129S1 mice were infected with $10^4$ PFU of MA-SARS-CoV-2 and treated for three days with 150 mg/kg of fluvoxamine, prior to harvesting lungs and collecting blood for viral titers and cytokine signature analysis, respectively. This virus has acquired several mutations through serial passaging in the lungs, mostly in the S protein, which allow the utilization of mouse ACE2 as a cellular receptor [20]. Over the course of the experiment, the weight of the animals did not show any significant change between the non-treated uninfected, the infected, and the treated groups (Fig. 5A). The analysis of lung viral titers at 3 dpi failed to show any significant changes in mice treated with fluvoxamine. Remdesivir was used as a positive control of antiviral activity [42,43] and produced a decrease in viral titers measured by $TCID_{50}$ (Fig. 5B). Cytokine multiplex assays showed increased levels of IL-6 and TNFα that decreased upon fluvoxamine treatment. In addition, the increased levels of the growth factors G-CSF

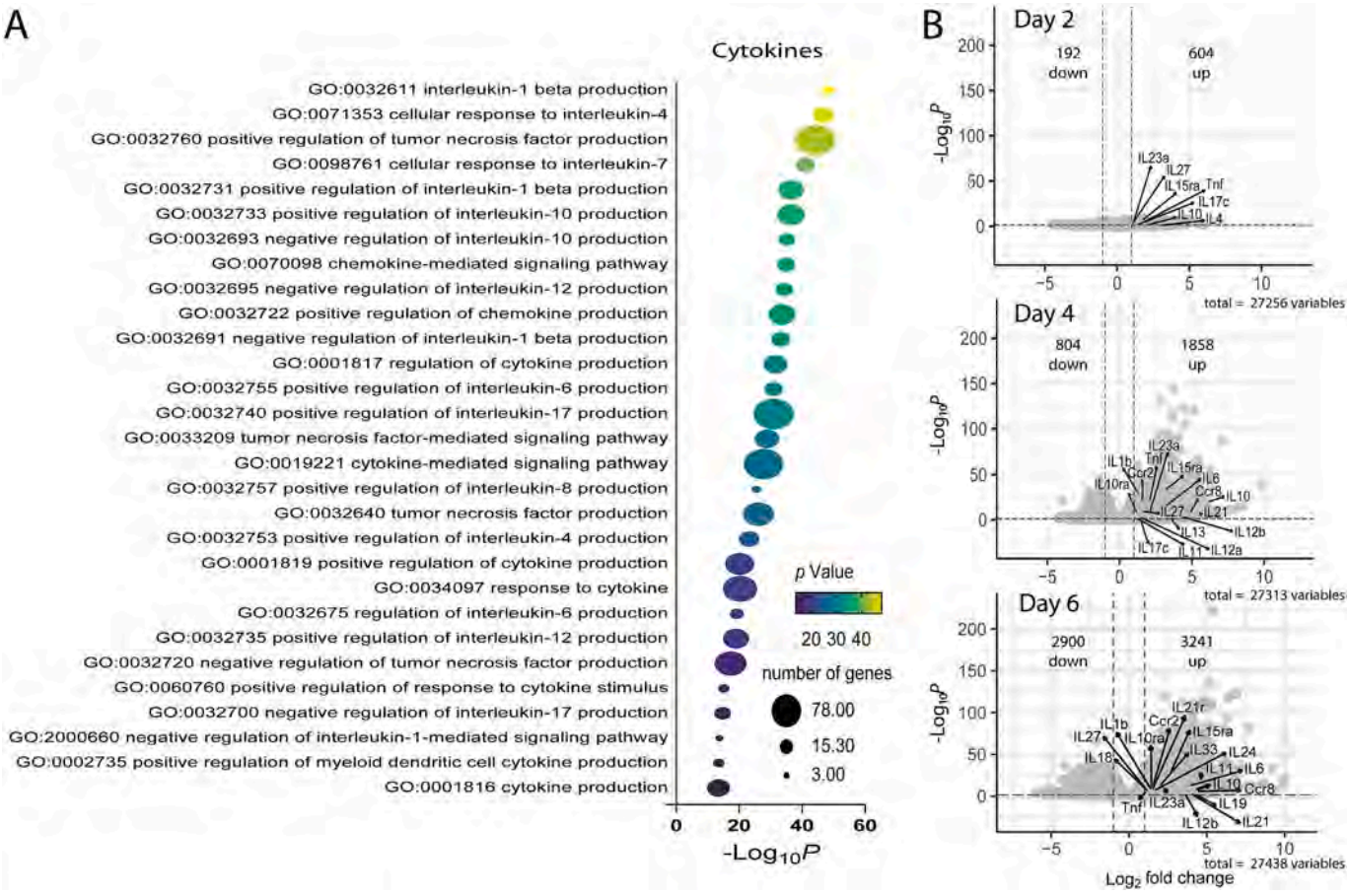


**Fig. 4.** Lungs of Syrian hamster infected with SARS-CoV-2 show increased levels of cytokines. (A) GO enriched pathways analysis and differential biological processes related to cytokines at 6 dpi. (B) Volcano plot of the cytokines showing significant changes at 2, 4, and 6 dpi.

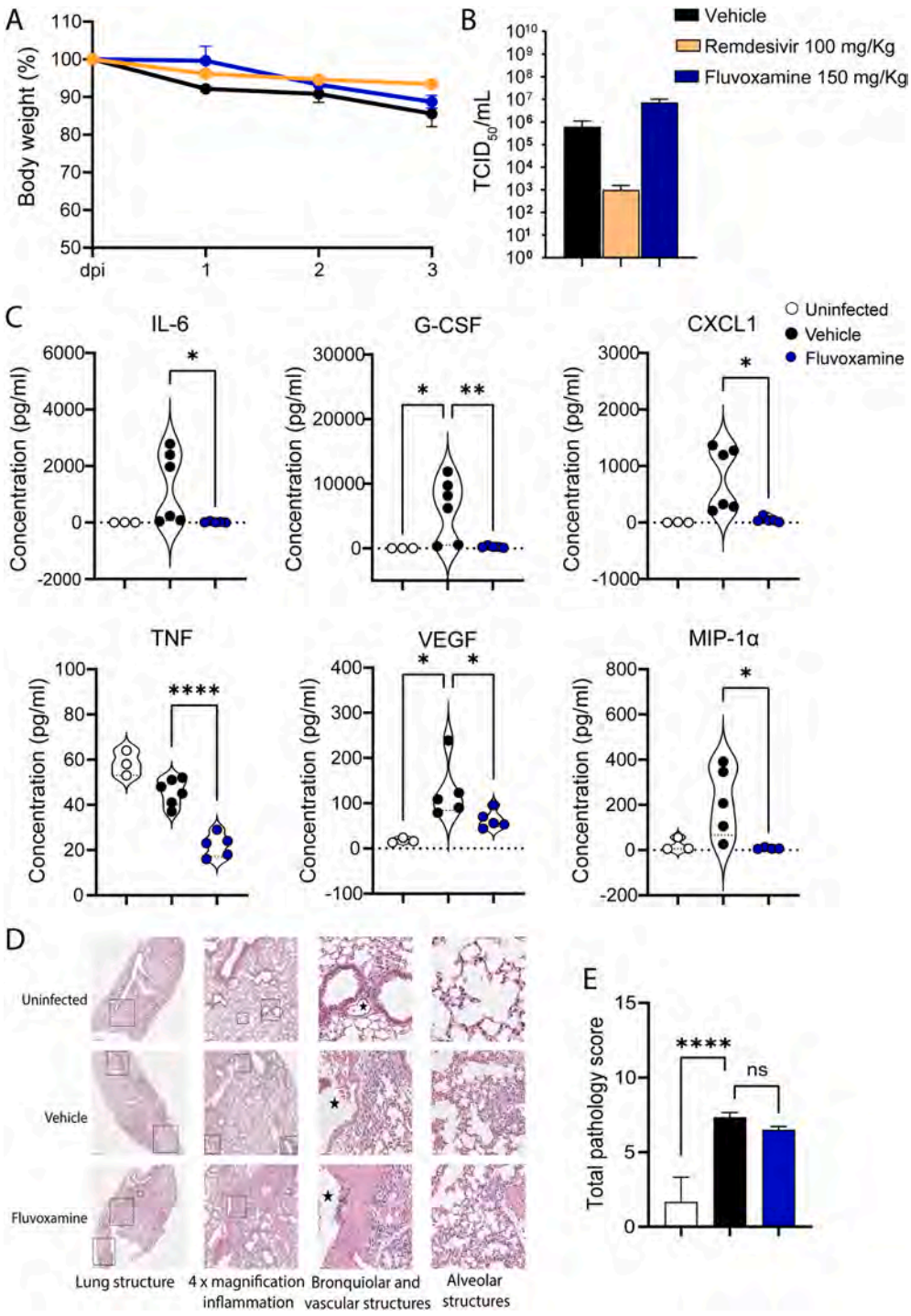


**Fig. 5.** Effect of fluvoxamine in 129S1 mice infected with MA-SARS-CoV-2. (A) 129S1 mice were infected with MA-SARS-CoV-2 at $10^4$ PFU and daily treated with 150 mg/kg s.c. fluvoxamine. Body weight was monitored throughout the experiment. (B) Viral titers measured by $TCID_{50}$. Mice treated with 100 mg/kg of remdesivir were used as an antiviral positive control. (C) Blood cytokine levels from 129S1 mice were assayed at 3 dpi using the MD44 Multiplex assay. Data are presented as mean ± SEM. *p < 0.05, **p < 0.01, ***$p$ < 0.005, ****$p$ < 0.001. Ordinary one-way ANOVA. (D) H&E-stained sections of a lung from a 10-week-old female 129S1 mice at 3 dpi. (E) Total pathology score was examined by implementing a semi-quantitative, 5-point grading scheme including four different histopathological parameters. Results only showed differences between uninfected, and vehicle and fluvoxamine-treated groups.

and VEGF observed during infection were countered by fluvoxamine treatment. The increase of MIP1α and CXCL1 levels was also thwarted by fluvoxamine treatment (Fig. 5C), while there were no significant changes in the levels of IL-10, IL-4, IFNβ, and IFNγ (Fig. S5A), several chemokines, and IL-1β (Fig. S5B and S5C). Infected and treated mice exhibited typical histopathological lesions of interstitial pneumonia in H&E-stained preparations measured by a semi-quantitative implementation for total pathology score (Fig. 5D and E). Overall, fluvoxamine counters the increased production of proinflammatory cytokines in peripheral blood during SARS-CoV-2 infection at early stages of infection, however, it does not exert any effect on viral replication and lung damage.

### 3.5. Role of CHOP, GADD34, and XBP1 during SARS-CoV-2 replication in human epithelial cells

Based on the *in vivo* results, experiments were designed for the analysis of global UPR activation during infection with SARS-CoV-2 WA1/2020 in A549-ACE2 cells at different MOI and timepoints. As observed in Fig. 6A, viral RNA increased in A549-ACE2 cells in correlation with the different MOI and timepoints. Increased levels of sXBP1 were observed up to 16 hpi, followed by a decrease at later times, independently of the MOI used (Fig. 6B), which agrees with an earlier report showing partial activation of IRE1α but not sXBP1 at 24 hpi [44]. The proteins of the PERK arm CHOP and GADD34 followed the same pattern of activation at early post-infection times, followed by a decrease at later times (Fig. 6C and D). To analyze the role of the different components of the UPR during virus replication, *DDIT3*, *GADD34*, and *XBP1* RNA expression were knocked down by RNA

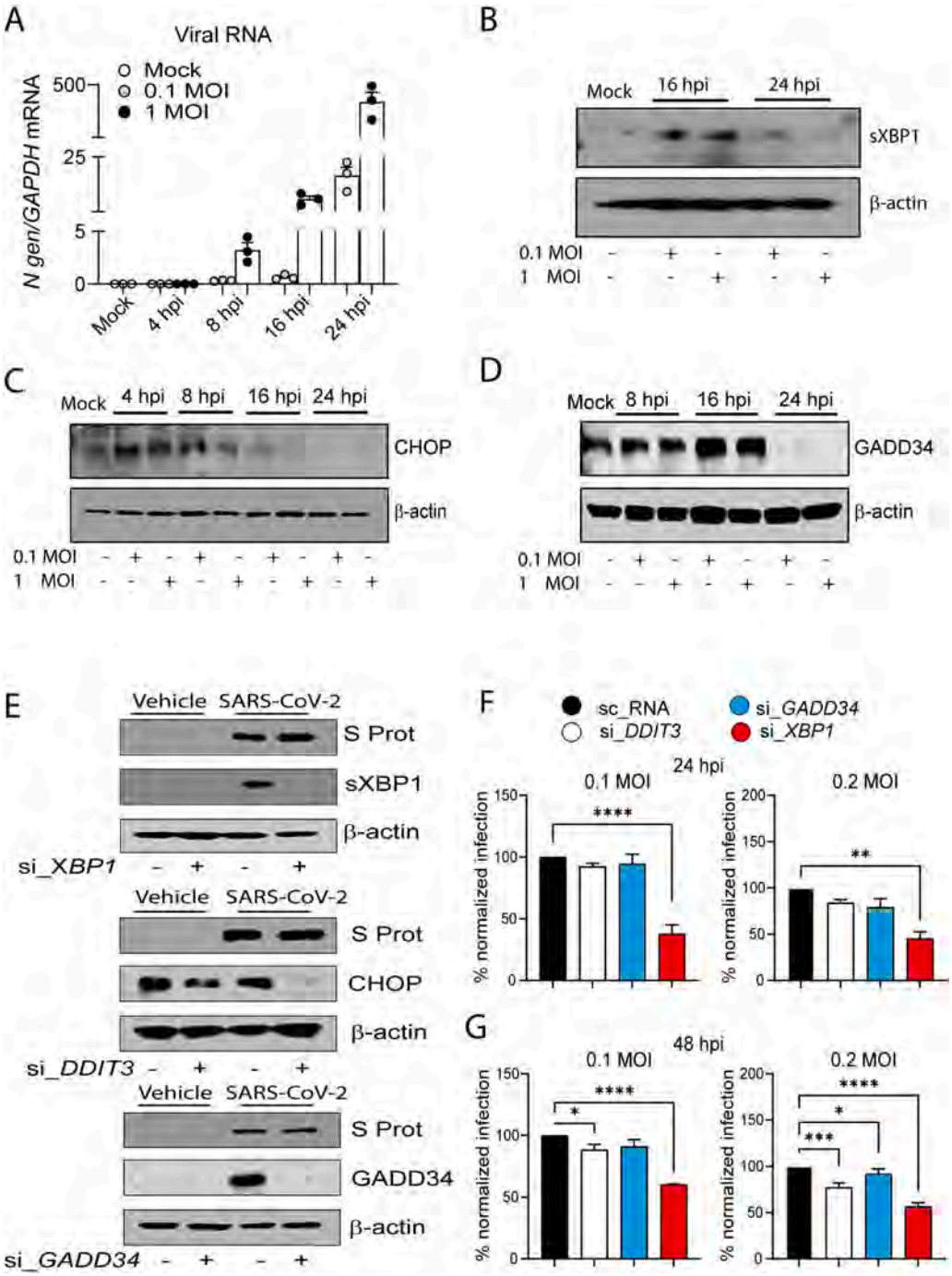


**Fig. 6.** Role of sXBP1, CHOP, and GADD34 during SARS-CoV-2 infection in A549-ACE2 human epithelial cells. (A) Viral load measured by RT-qPCR at different times after infection. (B-D) sXBP1, CHOP, and GADD34 protein expression. (E) 20 nM of siRNA were used to knockdown *DDIT3*, *GADD34*, and *XBP1* 24 h prior to infection with SARS-CoV-2 at 1 MOI for 16 h. After this time, protein extracts were collected for the immunodetection of S protein, DDIT3, GADD34, and sXBP1. (F-G) *DDIT3*, *GADD34*, and *XBP1* were knocked down 24 h before infection with SARS-CoV-2 under different MOI and timepoint conditions. Viral replication was assayed by immunostaining of N protein. The percentage of infection was quantified as (Infected cells/Total cells − Background) × 100, and the DMSO control was then set to 100 % infection for analysis. Data are presented as mean ± SEM of three biological replicates. *p < 0.05, **p < 0.01, ***p < 0.005, ****p < 0.001. Ordinary two-way ANOVA.

silencing. Cells were transfected for 24 h with 20 nM siRNA, prior to stimulation with 10 μM of tunicamycin, a pharmacological inducer of the three branches of the UPR. While tunicamycin increased CHOP, GADD34, and XBP1 protein expression, the siRNA treatment reduced their expression (Fig. S6A). Next, siRNAs transfected A549-ACE2 cells were infected with SARS-CoV-2 at 1 MOI for 16 h. Silencing of UPR proteins decreased their expression but not the viral S protein (Fig. 6E). Of note, virion release was reduced by *XBP1* knockdown at 48 hpi in cells infected at 0.1 MOI, but neither at earlier times nor upon transduction with siRNA targeting other UPR elements (Fig. S6B-S6D). Moreover, the analysis of infection assayed by immunostaining of the nucleocapsid (N) protein in A549-ACE2 cells undergoing *XBP1* knockdown decreased the percentage of infection at 0.1 and 0.2 MOI for 24 and 48 hpi (Fig. 6F and G). Similarly, *DDIT3* knockdown decreased infection at 48 hpi, and *GADD34* knockdown at 0.2 MOI and 48 hpi (Fig. 6G). Overall, infection of human epithelial cells with SARS-CoV-2 mimics *in vivo* findings, which postulates the IRE1α-XBP1 branch of the UPR as a pathogenetic trigger in SARS-CoV-2 infection.

### 3.6. Effect of different SARS-CoV-2 VOCs on UPR activity

SARS-CoV-2 VOCs have evolved since the beginning of the COVID-19 pandemic, and several variants of the ancestral SARS-CoV-2 have become dominant strains at different periods of time. These variants have specific changes in the S protein that produce increased affinity for the ACE2 receptor and/or immune evasion. It has been reported that the S protein can activate the three arms of the UPR [45–47], and this supports the need to address whether different VOCs exhibit distinct capacities to activate the UPR. HEK-293 T cells were transfected for 36 h with different plasmids encoding for different VOCs S proteins: wild-type (WT-D614G) [48], β (B1.351), γ (P.1), δ (B1.617.2), and omicron (BA.1 and BA.2). UPR target proteins HERPUD1 and sXBP1 were probed for UPR activation. Assays showed that all the S protein VOCs tested increased the UPR, in view of the upregulation of HERPUD1 and sXBP1 proteins (Fig. 7A). Moreover, sXBP1 protein and mRNA increased during the overexpression of VOC S proteins (Fig. 7B and C). The presence of three bands in some cases is explained by the formation of heteroduplexes (Fig. 7C). Although transfection of the different VOCs of the S protein could induce the IRE1α-XBP1 branch of the UPR, this assay might not replicate faithfully the conditions associated with infection.

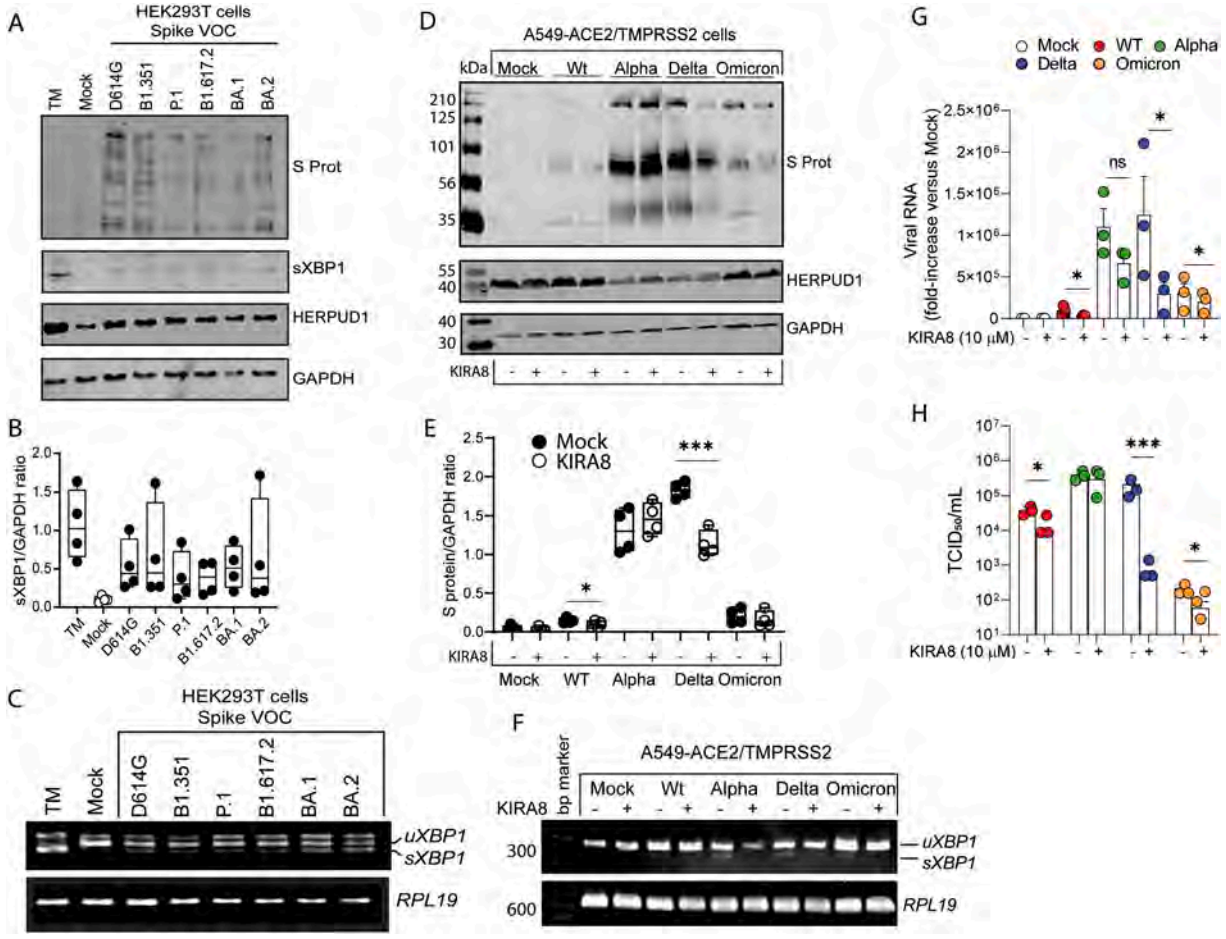


**Fig. 7.** Effect of different SARS-CoV-2 VOCs on the UPR. (A) HEK293 T cells were transfected with plasmids encoding SARS-CoV-2 S protein VOCs and harvested at 36 hpt for Western blot analysis of S protein, sXBP1, HERPUD1, and GAPDH proteins. Tunicamycin (TM) was used as a positive control for UPR activation. (B) Densitometric scanning of sXBP1 protein expression normalized to GAPDH in HEK293 T cells transfected and treated as in (A). (C) Analysis of *Xbp1* splicing by RT-PCR and agarose gel electrophoresis of HEK293 T cells treated as in (A). (D) A549-ACE2/TMPRSS2 cells were infected with SARS-CoV-2 VOCs at 0.1 MOI and incubated in the presence and absence of 10 μM KIRA8. Cell extracts were collected after 16 hpi for Western blot analysis of S protein, HERPUD1, and GAPDH. (E) Densitometric scanning of S protein. *$p < 0.05$. One sample *t*-test. ***$p < 0.001$. (F) Analysis of *Xbp1* splicing by RT-PCR and resolution in agarose gel of cells infected with different SARS-CoV-2 VOCs at 0.1 MOI for 16 hpi and treated in the presence and absence of 10 μM KIRA8. (G) Quantitation of viral RNA in A549-ACE2/TMPRSS2 infected cells. *N* gene was assayed for viral load quantitation and *RPL19* as a cell housekeeping gene. The IRE1α inhibitor KIRA8 was added immediately after the virus absorption period and maintained in the medium until cell harvesting 16 h later. (H) Viral titers measured by $TCID_{50}$. Immunoblots are representative of three independent biological replicates. Data are presented as mean ± SEM. *$p < 0.05$. ***$p < 0.001$. Paired Student's *t*-test.

Therefore, A549-ACE2/TMPRSS2 cells were infected at 0.1 MOI for 16 h with WT, α, δ, and omicron SARS-CoV-2 VOCs, following the addition of the specific inhibitor of the IRE1α-XBP1 branch KIRA8, which has been reported as a potent inhibitor of SARS-CoV-2 replication in Vero CCL81 and Calu-3 cells [47]. KIRA8 decreased viral replication, as deemed from the reduction of the expression of S protein in most of the infected cells, especially in the case of WT and δ (Fig. 7D and E). The expression of HERPUD1 protein was not affected by KIRA8 treatment and seemed to decrease in cells infected with the α and δ strains (Fig. 7D). KIRA8 also prevented the splicing of *XBP1* in infected cells (Fig. 7F), as well as viral RNA replication measured as SARS-CoV-2 *N* gene expression (Fig. 7G), concomitantly with the detection of lower viral titers (Fig. 7H). This was especially significant in the case of the δ variant. Viral RNA and titers in cells infected with the α variant were not reduced by KIRA8. These findings suggest that there might be a differential activation of the UPR in VOC-infected cells, most likely due to differences in replication kinetics or protein expression. In summary, the pharmacological manipulation of the IRE1α-XBP1 branch significantly inhibits SARS-CoV-2 replication with different VOCs. This indicates that the IRE1α-XBP1 branch might be a critical pathway involved in the replication cycle of SARS-CoV-2 infection.

## 4. Discussion

SARS-CoV-2 uses host immune responses to ensure replication and the ensuing inflammatory response. This includes leveraging ER stress for proliferation [47,49]. A breakthrough into the mechanism of SARS-CoV-2 proliferation cycle has been unveiling the ability of the IRE1α-XBP1 arm to maintain the levels of NUAK2 kinase in Calu-3 human epithelial cells. NUAK2 regulates the cell surface levels of viral receptors. This allows viral entry and the intercellular transmission of the UPR *via* the secretion of soluble messengers and lends support to the involvement of the UPR in viral replication. The finding of a 2.112-fold-increase of *Nuak2* mRNA expression at 6 dpi in the hamster model (Fig. 3B and C) agrees with that report. In contrast, we have not observed induction of the PERK-dependent gene *Gadd34* in the animal models of infection, while this was the UPR target gene showing a most prominent induction in Calu-3 cells [27]. A comparative analysis of the transcriptome induced by SARS-CoV-2 Syrian hamster and K18-hACE2 mouse with Prasad et al. report [27] disclosed a low number of transcripts shared with Calu-3 cells (Fig. S7). This can be explained by species and cell type differences and disparity in the annotation of the genomes since human is the best annotated genome and genes that are activated in humans might not be annotated in mouse/hamster or show different names. The present study also uncovers a low number of genes showing a similar regulation by UPR-inducing drugs and SARS-CoV-2 infection. Consistent with the significance of these experimental data, sXBP1 protein has been detected in sera from patients with severe COVID-19 pneumonia [49], as well as increased plasma levels of GRP78, the protein encoded by the gene *HSPA5* [50]. These data agree with early studies showing the activation of the IRE1α-XBP1 arm in monocytes and the association of $XBP1^{+}$ plasma B cells with COVID-19 pneumonia severity [51].

In this study, we disclosed the activity of the Ire1α-Xbp1 branch after a systematic approach in *in vivo* models showing distinct clinic manifestations and in cell lines. The most prominent activation of the UPR was observed in K18-hACE2 mice and Syrian hamsters as compared to mice previously transduced with the human ACE2 receptor in C57BL/6 and BALB/c backgrounds. In particular, the Ire1α-Xbp1 arm was upregulated and paralleled the overproduction of cytokines in acute infection, while *Ddit3* mRNA and Chop protein were not influenced by infection in both K18-hACE2 and Syrian hamster. The scrutiny of the function of the innate immune system in Syrian hamsters showed a robust stimulation of TLR-dependent signaling, which agrees with previous reports showing that TLR2 recognizes S and envelope (E) proteins of SARS-CoV-2 and induces the production of proinflammatory cytokines [52–54]. Unlike TLR3 and the cytoplasmic receptors RIG-I and MDA5, the endosomal tandem TLR7/8 recognizes viral ssRNAs, which makes this receptor system most appropriate for triggering the innate response to viral patterns. While TLR8 induces cytokine and chemokine genes in the human monocyte-macrophage lineage, TLR7 exerts this function in mice [55]. In line with this, a recent study addressing the pathophysiology of CS disclosed that plasmacytoid dendritic cells (pDC) are the sole cell type able to generate IFNα *via* TLR7 after sensing SARS-CoV-2 in human blood, while macrophages produce IFNα only when in physical contact with infected epithelial cells. Of note, pDC-derived IFNα elicits changes in macrophages at both transcriptional and epigenetic levels, which drive hyperactivation in response to TLR3 and TLR8 ligands [56]. These data agree with the robust expression of *TLR8* and monocytic lineage markers mRNA in bronchioloalveolar aspirates of patients with severe COVID-19 pneumonia, concomitantly with the detection of proinflammatory cytokines and *sXBP1* and the TLR8- and *sXBP1*-dependent induction of cytokines in monocyte-derived dendritic cells produced by ssRNA40 [57], a synthetic mimic of ssRNA guanine- and uracil-rich sequences included in SARS-CoV-2 RNA [58,59]. Tellingly, a recent immunoinformatic analysis showed that the SARS-CoV-2 genome has more ssRNA portions that could be recognized by TLR7/8 than SARS-CoV and MERS-CoV genomes [60]. These data extend to TLR8 the supportive role of sXbp1 in the induction of proinflammatory proteins associated with TLR2 and TLR4 stimulation [5,61].

Fluvoxamine was used to test the effect of a repurposed immunomodulator in the control of SARS-CoV-2 infection, in view of the reported role of SSRIs on viral proliferation, viral titers, and cytokine expression [62–64]. The effect of SIR1 on the UPR was associated with its capacity to counteract cytokine induction in bacterial sepsis [65]. Hence, we posited that fluvoxamine could target UPR-dependent cytokine induction and viral replication, although SSRIs affect different targets. In fact, a recent study associated the antiviral and anti-inflammatory properties of the parent compound fluoxetine with the inhibition of acid sphingomyelinase [66]. Since fluvoxamine did not show any effect on viral replication, it seems likely that the mechanism whereby it might influence the course of COVID-19 infection is associated with ER stress [67]. Several reports underscore the contribution of the UPR to viral replication in SARS-CoV-2 infected cell lines [44,46,47,68,69]. In contrast, up-regulation of IRE1α RNase activity by cannabidiol has been found to block SARS-CoV-2 replication in A549-ACE2 cells and in nasal turbinates of infected mice [70]. Our findings extend to *in vivo* models the robust activation of the IRE1α-XBP1 arm of the UPR observed in patients with COVID-19 disease. It is also shown that transfection of different S protein VOCs and infection with SARS-CoV-2 increases sXBP1 mRNA and protein, while the IRE1α RNase inhibitor KIRA8 counters these effects and reduces viral replication. This agrees with a recent report revealing that systemic candidiasis in conditional-KO mice lacking IRE1α in leukocytes showed a 25 % survival rate, while their IRE1α-sufficient counterparts died before 15 dpi. Treatment with MKC8866, which specifically targets the RNase domain of IRE1α, also mitigated kidney inflammation and prolonged survival. A comparative analysis of the transcriptomes observed in the current study with that reported in mouse candidiasis shows a similar pattern of Ire1α-dependent expression of genes, *i.e.*, *Hspa5*, *Dnajb9*, and *Sec61a1*, as well as reduction of IL6, CCL5, TNFα, and MIP1α proteins [71]. Based on these data, the present study suggests that targeting IRE1α may be a promising target for SARS-CoV-2 pneumonia.

## CRediT authorship contribution statement

**Jose Javier Fernández:** Methodology, Investigation, Conceptualization. **Arturo Marín:** Methodology, Investigation, Formal analysis, Data curation, Conceptualization. **Romel Rosales:** Conceptualization, Investigation, Methodology. **Rebekah Penrice-Randal:** Conceptualization, Funding acquisition, Investigation, Validation. **Petra Mlcochova:** Data curation, Investigation. **Fernando Villalón-Letelier:**

Conceptualization, Investigation, Methodology, Resources. **Soner Yildiz:** Conceptualization, Investigation. **Enrique Pérez:** Software. **Raveen Rathnasinghe:** Supervision, Methodology, Conceptualization, Data curation, Investigation. **Anastasija Cupic:** Investigation, Methodology. **Thomas Kehrer:** Supervision, Methodology, Investigation, Conceptualization. **Melissa B. Uccellini:** Methodology, Investigation. **Sara Alonso:** Investigation. **Fernando Martínez:** Investigation. **Briana Lynn McGovern:** Conceptualization, Data curation, Investigation, Methodology, Resources. **Jordan J. Clark:** Methodology, Investigation, Conceptualization. **Parul Sharma:** Supervision, Resources, Investigation. **Yolanda Bayón:** Investigation, Conceptualization. **Andrés Alonso:** Investigation. **Randy A. Albrecht:** Methodology, Investigation, Formal analysis, Data curation, Conceptualization. **Kris M. White:** Investigation, Funding acquisition, Formal analysis, Conceptualization. **Michael Schotsaert:** Conceptualization, Data curation, Formal analysis, Funding acquisition, Investigation, Methodology, Project administration, Resources. **Lisa Miorin:** Conceptualization, Data curation, Formal analysis, Funding acquisition, Investigation, Methodology, Resources, Supervision, Validation, Writing – original draft. **James P. Stewart:** Validation, Resources, Investigation, Conceptualization, Data curation. **Julian A. Hiscox:** Validation, Supervision, Resources, Investigation, Funding acquisition, Conceptualization. **Ravindra K. Gupta:** Validation, Supervision, Resources, Funding acquisition, Conceptualization. **Nerea Irigoyen:** Formal analysis, Data curation, Conceptualization, Investigation, Methodology, Resources, Supervision, Visualization, Writing – original draft, Funding acquisition. **Adolfo García-Sastre:** Writing – review & editing, Writing – original draft, Visualization, Conceptualization, Data curation, Formal analysis, Funding acquisition, Investigation, Methodology, Project administration, Resources, Supervision, Validation. **Mariano Sánchez Crespo:** Writing – review & editing, Writing – original draft, Visualization, Validation, Supervision, Resources, Project administration, Methodology, Investigation, Funding acquisition, Data curation, Conceptualization. **Nieves Fernández:** Writing – original draft, Conceptualization, Investigation, Project administration, Resources.

## Declaration of competing interest

The A.G.S. laboratory has received research support from GSK, Pfizer, Senhwa Biosciences, Kenall Manufacturing, Blade Therapeutics, Avimex, Johnson & Johnson, Dynavax, 7Hills Pharma, Pharmamar, ImmunityBio, Accurius, Nanocomposix, Hexamer, N-fold LLC, Model Medicines, Atea Pharma, Applied Biological Laboratories and Merck, outside of the reported work. A.G.S. has consulting agreements for the following companies involving cash and/or stock: Castlevax, Amovir, Vivaldi Biosciences, Contrafect, 7Hills Pharma, Avimex, Pagoda, Accurius, Esperovax, Farmak, Applied Biological Laboratories, Pharmamar, CureLab Oncology, CureLab Veterinary, Synairgen, Paratus and Pfizer, outside of the reported work. A.G.S. has been an invited speaker in meeting events organized by Seqirus, Janssen, Abbott and Astrazeneca. A.G.S is inventor on patents and patent applications on the use of antivirals and vaccines for the treatment and prevention of virus infections and cancer, owned by the Icahn School of Medicine at Mount Sinai, New York, outside of the reported work. A.M. is the creator of Omics Bioinformatics S.L. and owns all the stocks of this company. The M.S. laboratory has received unrelated research funding in sponsored research agreements from 7Hills Pharma, ArgenX N.V., Moderna and Phio Pharmaceuticals, which has no competing interest with this work. The article reflects the views of the authors and does not represent the views or policies of the FDA. All other authors declare that they have no conflict of interest.

## Data availability

K18-hACE2 bioinformatics data are available under BioProject ID: PRJNA914664 on Short Read Archive (SRA). Hamster data were stored in the NCBI (NCBI Bioproject database under accession number PRJNA952603 and NCBI GEO accession GSE230130 and will be accessible once the article is published.

*Acknowledgments*

The authors thank the EMBO Scientific Exchange Grant and EFIS-IL Short-term Fellowship and G2P-UK National Virology consortium funded by MRC/UKRI (grant ref.: MR/W005611/1) and the Barclay Lab at Imperial College for providing the following material: pcDNA3.1-S protein-D614G-D19; pcDNA3.1-S protein-B1.351-D19; pcDNA3.1-S protein-P1-D19; pcDNA3.1-S protein-B1.617.2-D19; pcDNA3.1-S protein-BA.1-D19; pcDNA3.1-S protein-BA.2-D19. Lineage B SARS-CoV-2/human/Liverpool/REMRQ0001/2020 was a kind gift from Ian Goodfellow, previously isolated by Lance Turtle (University of Liverpool), David Matthews and Andrew Davidson (University of Bristol). B.1.1.7; SARS-CoV-2 England/ATACCC 174/2020 was a gift from G. Towers. Lineages B.1.1.617.2 (Delta, GISAID: EPI_ISL_1731019) and B.1.1.529 (Omicron UK isolate, G. Screaton) were received as part of the work conducted by G2P-UK National Virology Consortium. Bulk RNA Sequencing sample libraries for the experiment in golden Syrian hamsters were prepared and sequenced at the Center for Advanced Genomics Technology Facility directed by Dr. Robert Sebra at ISMMS. The authors are grateful for the help of Gagandeep Singh in the elaboration of the Venn diagrams. BioRender.com software was used in the Graphical Abstract.

*Funding*

This work was supported by Junta de Castilla y León/Fondo Social Europeo Grants CSI035P17 (M.S.C.) and VA175P20 (N.F.). Fondo COVID-19 del Instituto de Salud Carlos III/Junta de Castilla y León. European Commission-NextGenerationEU, (Regulation EU 2020/2094), through CSIC's Global Health Platform (PTI Salud Global). Plan Nacional de Salud y Farmacia Grant SAF2017-83079-R and Grant PID2020-113751RB-I00 funded by MCIN/AEI/ 10.13039/501100011033 (J.J. F., M.S.C., N.F.). Wellcome Trust Senior Fellowship in Clinical Science (WT108082AIA) (P.M., R.K.G.). U.S. Food and Drug Administration Medical Countermeasures Initiative contract (75F40120C00085) (J.A. H.). MRC (MR/W005611/1) G2P-UK: A national virology consortium to address phenotypic consequences of SARS-CoV-2 genomic variation (co-Is JPS and JAH). National Institutes of Health (NIH) grant: R21AI147172 (N.I.), NIH/NIAID R01AI160706, NIH/NIAID R21AI176069, and NIH/NIDDK R01DK130425 (M.S.). This work was also partly supported by NIAID grant U19AI135972, and by CRIPT (Center for Research on Influenza Pathogenesis and Transmission), a NIAID funded Center of Excellence for Influenza Research and Response (CEIRR, contract # 75N93021C00014) (A.G.S.). This work was supported in part through the computational resources and staff expertise provided by Scientific Computing at the Icahn School of Medicine at Mount Sinai and supported by the Clinical and Translational Science Awards (CTSA) grant UL1TR004419 from the National Center for Advancing Translational Sciences.

## Appendix A. Supplementary data

Supplementary data to this article can be found online at https://doi.org/10.1016/j.bbadis.2024.167193.

## References

[1] P. V'kovski, A. Kratzel, S. Steiner, H. Stalder, V. Thiel, Coronavirus biology and replication: implications for SARS-CoV-2, Nat. Rev. Microbiol. 19 (2021) 155–170, https://doi.org/10.1038/s41579-020-00468-6.

[2] A. Lmanza, A. Carlesso, C. Chintha, S. Creedican, D. Doultsinos, B. Leuzzi, A. Luís, N. McCarthy, L. Montibeller, S. More, Endoplasmic reticulum stress

signalling–from basic mechanisms to clinical applications, FEBS J. 286 (2019) 241–278, https://doi.org/10.1111/febs.14608.
[3] J. Grootjans, A. Kaser, R.J. Kaufman, R.S. Blumbergn, The unfolded protein response in immunity and inflammation, Nat. Rev. Immunol. 16 (2016) 469–484, https://doi.org/10.1038/nri.2016.62.
[4] N.N. Iwakoshi, A.H. Lee, L.H. Glimcher, The X-box binding protein-1 transcription factor is required for plasma cell differentiation and the unfolded protein response, Immunol. Rev. 194 (2003) 29–38, https://doi.org/10.1034/j.1600-065x.2003.00057.x.
[5] F. Martinon, X. Chen, A.H. Lee, L.H. Glimcher, TLR activation of the transcription factor XBP1 regulates innate immune responses in macrophages, Nat. Immunol. 11 (2010) 411–418, https://doi.org/10.1038/ni.1857.
[6] F. Chen, L. Hao, S. Zhu, X. Yang, W. Shi, K. Zheng, T. Wang, H. Chen, Potential adverse effects of dexamethasone therapy on COVID-19 patients: review and recommendations, Infect. Dis. Ther. 10 (2021) 1907–1931, https://doi.org/10.1007/s40121-021-00500-z.
[7] X. Xu, M. Han, T. Li, W. Sun, D. Wang, B. Fu, Y. Zhou, X. Zheng, Y. Yang, X. Li, X. Zhang, A. Pan, H. Wei, Effective treatment of severe COVID-19 patients with tocilizumab, Proc. Natl. Acad. Sci. U. S. A. 117 (2020) 10970–10975, https://doi.org/10.1073/pnas.2005615117.
[8] G. Reis, E.A. Dos Santos Moreira-Silva, D.C.M. Silva, L. Thabane, A.C. Milagres, T. S. Ferreira, C.V.Q. Dos Santos, V.H. de Souza Campos, A.M.R. Nogueira, A.P.F.G. de Almeida, E.D. Callegari, A.D. de Figueiredo Neto, L.C.M. Savassi, M.I.C. Simplicio, L.B. Ribeiro, R. Oliveira, O. Harari, J.I. Forrest, H. Ruton, S. Sprague, P. McKay, A. V. Glushchenko, C.R. Rayner, E.J. Lenze, A.M. Reiersen, G.H. Guyatt, E.J. Mills, TOGETHER investigators, effect of early treatment with fluvoxamine on risk of emergency care and hospitalisation among patients with COVID-19: the TOGETHER randomised, platform clinical trial, lancet glob, Health 10 (2022) e42–e51, https://doi.org/10.1016/S2214-109X(21)00448-4.
[9] T.C. Lee, S. Vigod, E. Bortolussi-Courval, R. Hanula, D.R. Boulware, E.J. Lenze, A. M. Reiersen, E.G. McDonald, Fluvoxamine for outpatient management of COVID-19 to prevent hospitalization: a systematic review and meta-analysis, JAMA Netw. Open 5 (2022) e226269, https://doi.org/10.1001/jamanetworkopen.2022.6269.
[10] D.E. Gordon, G.M. Jang, M. Bouhaddou, J. Xu, K. Obernier, K.M. White, M. J. O'Meara, V.V. Rezelj, J.Z. Guo, A SARS-CoV-2 protein interaction map reveals targets for drug repurposing, Nature 583 (2020) 459–468, https://doi.org/10.1038/s41586-020-2286-9.
[11] D.E. Gordon, J. Hiatt, M. Bouhaddou, V.V. Rezelj, S. Ulferts, H. Braberg, A. S. Jureka, K. Obernier, J. Guo, et al., Comparative host-coronavirus protein interaction networks reveal pan-viral disease mechanisms, Science 370 (2020), https://doi.org/10.1126/science.abe9403 eabe9403.
[12] J.M. Vela, Repurposing sigma-1 receptor ligands for COVID-19 therapy? Front. Pharmacol. 11 (2020) 582310 https://doi.org/10.3389/fphar.2020.582310.
[13] C. Abate, M. Niso, F.S. Abatematteo, M. Contino, N.A. Colabufo, F. Berardi, PB28, the sigma-1 and sigma-2 receptors modulator with potent anti–SARS-CoV-2 activity: a review about its pharmacological properties and structure affinity relationships, Front. Pharmacol. 11 (2020) 589810, https://doi.org/10.3389/fphar.2020.589810.
[14] K. Hashimoto, Repurposing of CNS drugs to treat COVID-19 infection: targeting the sigma-1 receptor, Eur Arch Psychiatry Clin.Neurosci 271 (2021) 249–258, https://doi.org/10.1007/s00406-020-01231-x.
[15] Z. Daniloski, T.X. Jordan, H.H. Wessels, D.A. Hoagland, S. Kasela, M. Legut, S. Maniatis, E.P. Mimitou, L. Lu, E. Geller, O. Danziger, B.R. Rosenberg, H. Phatnani, P. Smibert, T. Lappalainen, B.R. Tenoever, N.E. Sanjana, Identification of required host factors for SARS-CoV-2 infection in human cells, Cell 184 (2021) 92–105.e16, https://doi.org/10.1016/j.cell.2020.10.030.
[16] S.J. Rihn, A. Merits, S. Bakshi, M.L. Turnbull, A. Wickenhagen, A.J.T. Alexander, C. Baillie, B. Brennan, F. Brown, K. Brunker, et al., A plasmid DNA-launched SARS-CoV-2 reverse genetics system and coronavirus toolkit for COVID-19 research, PLoS Biol. 19 (2021) e3001091, https://doi.org/10.1371/journal.pbio.3001091.
[17] A.K. Reuschl, L.G. Thorne, L. Zuliani-Alvarez, M. Bouhaddou, K. Obernier, J. Hiatt, M. Soucheray, J. Turner, J.M. Fabius, G.T. Nguyen, Host-directed therapies against early-lineage SARS-CoV-2 retain efficacy against B. 1.1. 7 variant, BioRxiv (2021), https://doi.org/10.1101/2021.01.24.427991.
[18] W. Dejnirattisai, J. Huo, D. Zhou, J. Zahradník, P. Supasa, C. Liu, H.M. Duyvesteyn, H.M. Ginn, A.J. Mentzer, A. Tuekprakhon, SARS-CoV-2 omicron-B. 1.1. 529 leads to widespread escape from neutralizing antibody responses, Cell 185 (2022) 467–484, https://doi.org/10.1016/j.cell.2021.12.046.
[19] R. Nutalai, D. Zhou, A. Tuekprakhon, H.M. Ginn, P. Supasa, C. Liu, J. Huo, A. J. Mentzer, H.M. Duyvesteyn, A. Dijokaite-Guraliuc, Potent cross-reactive antibodies following omicron breakthrough in vaccinees, Cell 185 (2022) 2116–2131, https://doi.org/10.1016/j.cell.2022.05.014.
[20] R. Rathnasinghe, S. Jangra, C. Ye, A. Cupic, G. Singh, C. Martínez-Romero, L.C. F. Mulder, T. Kehrer, D.S. Yildiz, A. Choi, S.T. Yeung, I. Mena, V. Gillespie, J. De Vrieze, S. Aslam, D. Stadlbauer, D.A. Meekins, C.D. McDowell, V. Balaraman, M. J. Corley, J.A. Richt, B.G. De Geest, L. Miorin, PVI study group, F. Krammer, L. Martinez-Sobrido, V. Simon, A. García-Sastre, M. Schotsaert, Characterization of SARS-CoV-2 spike mutations important for infection of mice and escape from human immune sera, Nat. Commun. 13 (2022) 3921, https://doi.org/10.1038/s41467-022-30763-0 (PMID: 35798721).
[21] J.J. Clark, R. Penrice-Randal, P. Sharma, A. Kipar, X. Dong, S.H. Pennington, A.E. Marriott, S. Colombo, A. Davidson, M.K. Williamson, Sequential infection with influenza a virus followed by severe acute respiratory syndrome coronavirus 2 (SARS-CoV-2) leads to more severe disease and encephalitis in a mouse model of COVID-19, BioRxiv, doi:https://doi.org/10.1101/2020.10.13.334532.
[22] A. Dobin, C.A. Davis, F. Schlesinger, J. Drenkow, C. Zaleski, S. Jha, P. Batut, M. Chaisson, T.R. Gingeras, STAR: ultrafast universal RNA-seq aligner, Bioinformatics 29 (2013) 15–21, https://doi.org/10.1093/bioinformatics/bts635.
[23] M.I. Love, W. Huber, S. Anders, Moderated estimation of fold change and dispersion for RNA-seq data with DESeq2, Genome Biol. 15 (15) (2014) 550, https://doi.org/10.1186/s13059-014-0550-8.
[24] M.D. Robinson, D.J. McCarthy, G.K. Smyth, edgeR: a Bioconductor package for differential expression analysis of digital gene expression data, Bioinformatics 26 (2010) 139–140, https://doi.org/10.1093/bioinformatics/btp616.
[25] D. Wu, G.K. Smyth, Camera: a competitive gene set test accounting for inter-gene correlation, Nucleic Acids Res. 40 (2012) e133, https://doi.org/10.1093/nar/gks461.
[26] Y. Zhang, C. Park, C. Bennett, M. Thornton, D. Kim, Rapid and accurate alignment of nucleotide conversion sequencing reads with HISAT-3N, Genome Res. 31 (2021) 1290–1295, https://doi.org/10.1101/gr.275193.120.
[27] V. Prasad, B. Cerikan, Y. Stahl, K. Kopp, V. Magg, N. Acosta-Rivero, H. Kim, K. Klein, C. Funaya, U. Haselmann, M. Cortese, F. Heigwer, J. Bageritz, D. Bitto, S. Jargalsaikhan, C. Neufeldt, F. Pahmeier, M. Boutros, Y. Yamauchi, A. Ruggieri, R. Bartenschlager, Enhanced SARS-CoV-2 entry via UPR-dependent AMPK-related kinase NUAK2, Mol. Cell 83 (2023) 2559–2577.e8, https://doi.org/10.1016/j.molcel.2023.06.020.
[28] F. Amanat, K.M. White, L. Miorin, S. Strohmeier, M. McMahon, P. Meade, W.C. Liu, R.A. Albrecht, V. Simon, L. Martinez-Sobrido, An in vitro microneutralization assay for SARS-CoV-2 serology and drug screening, Curr. Protoc. Microbiol. 58 (2020) e108, https://doi.org/10.1002/cpmc.108.
[29] M.J. Kuiper, L.O.W. Wilson, S. Mangalaganesh, C. Lee, D. Reti, S.S. Vasan, But mouse, you are not lone": on some severe acute respiratory syndrome coronavirus 2 variants infecting mice, ILAR J 262 (2021) 48–59, https://doi.org/10.1093/ilar/ilac002.
[30] R. Rathnasinghe, S. Strohmeier, F. Amanat, V.L. Gillespie, F. Krammer, A. García-Sastre, L. Coughlan, M. Schotsaert, M.B. Uccellini, Comparison of transgenic and adenovirus hACE2 mouse models for SARS-CoV-2 infection, Emerg. Microbes Infect. 9 (2020) 2433–2445, https://doi.org/10.1080/22221751.2020.1838955.
[31] I.M. Ibrahim, D.K. Abdelmalek, M.E. Elshahat, A.A. Elfiky, COVID-19 spike-host cell receptor GRP78 binding site prediction, J. Infect. 80 (2020) 554–562, https://doi.org/10.1016/j.jinf.2020.02.026.
[32] W.J. Shin, D.P. Ha, K. Machida, A.S. Lee, The stress-inducible ER chaperone GRP78/BiP is upregulated during SARS-CoV-2 infection and acts as a pro-viral protein, Nat. Commun. 13 (2022) 1–6, https://doi.org/10.1038/s41467-022-34065-3.
[33] N. Liu, C. Jiang, P. Cai, Z. Shen, W. Sun, H. Xu, M. Fang, X. Yao, L. Zhu, X. Gao, Single-cell analysis of COVID-19, sepsis, and HIV infection reveals hyperinflammatory and immunosuppressive signatures in monocytes, Cell Rep, 37: 109793. doi: https://doi.org/10.1016/j.celrep.2021.109793.
[34] C. Hetz, K. Zhang, R.J. Kaufman, Mechanisms, regulation and functions of the unfolded protein response, Nat. Rev. Mol. Cell Biol. 21 (2021) 421–438, https://doi.org/10.1038/s41580-020-0250-z.
[35] J.F. Chan, A.J. Zhang, S. Yuan, V.K. Poon, C.C. Chan, A.C. Lee, W.M. Chan, Z. Fan, H.W. Tsoi, L. Wen, R. Liang, J. Cao, Y. Chen, K. Tang, C. Luo, J.P. Cai, K.H. Kok, H. Chu, K.H. Chan, S. Sridhar, Z. Chen, H. Chen, K.K. To, K.Y. Yuen, Simulation of the clinical and pathological manifestations of coronavirus disease 2019 (COVID-19) in a golden Syrian hamster model: implications for disease pathogenesis and transmissibility, Clin. Infect. Dis. 71 (2020) 2428–2446, https://doi.org/10.1093/cid/ciaa325.
[36] M. Imai, K. Iwatsuki-Horimoto, M. Hatta, S. Loeber, P.J. Halfmann, N. Nakajima, T. Watanabe, M. Ujie, K. Takahashi, M. Ito, S. Yamada, S. Fan, S. Chiba, M. Kuroda, L. Guan, K. Takada, T. Armbrust, A. Balogh, Y. Furusawa, M. Okuda, H. Ueki, A. Yasuhara, Y. Sakai-Tagawa, T.J.S. Lopes, M. Kiso, S. Yamayoshi, N. Kinoshita, N. Ohmagari, S.I. Hattori, M. Takeda, H. Mitsuya, F. Krammer, T. Suzuki, Y. Kawaoka, Syrian hamsters as a small animal model for SARS-CoV-2 infection and countermeasure development, Proc. Natl. Acad. Sci. U. S. A. 117 (2020) 16587–16595, https://doi.org/10.1073/pnas.2009799117.
[37] T.M. Mogensen, IRF and STAT transcription factors-from basic biology to roles in infection, protective immunity, and primary immunodeficiencies, Front. Immunol. 9 (2019) 3047, https://doi.org/10.3389/fimmu.2018.03047.
[38] H. Xia, Z. Cao, X. Xie, X. Zhang, J.Y. Chen, H. Wang, V.D. Menachery, R. Rajsbaum, P.Y. Shi, Evasion of type I interferon by SARS-CoV-2, Cell Rep. 33 (2020) 108234, https://doi.org/10.1016/j.celrep.2020.108234.
[39] E.J. Lenze, C. Mattar, C.F. Zorumski, A. Stevens, J. Schweiger, G.E. Nicol, J. P. Miller, L. Yang, M. Yingling, M.S. Avidan, A.M. Reiersen, Fluvoxamine vs placebo and clinical deterioration in outpatients with symptomatic COVID-19: a randomized clinical trial, JAMA 324 (2020) 2292–2300, https://doi.org/10.1001/jama.2020.22760.
[40] A. Szabo, A. Kovacs, E. Frecska, E. Rajnavolgyi, Psychedelic N, N-dimethyltryptamine and 5-methoxy-N, N-dimethyltryptamine modulate innate and adaptive inflammatory responses through the sigma-1 receptor of human monocyte-derived dendritic cells, PloS One 9 (2014) e106533, https://doi.org/10.1371/journal.pone.0106533.
[41] M. Ghareghani, K. Zibara, H. Sadeghi, S. Dokoohaki, H. Sadeghi, R. Aryanpour, A. Ghanbari, Fluvoxamine stimulates oligodendrogenesis of cultured neural stem cells and attenuates inflammation and demyelination in an animal model of multiple sclerosis, Sci. Rep. 7 (2017) 1–17, https://doi.org/10.1038/s41598-017-04968-z.
[42] B.N. Williamson, F. Feldmann, B. Schwarz, K. Meade-White, D.P. Porter, J. Schulz, N. van Doremalen, I. Leighton, C.K. Yinda, L. Pérez-Pérez, A. Okumura, J. Lovaglio, P.W. Hanley, G. Saturday, C.M. Bosio, S. Anzick, K. Barbian, T. Cihlar, C. Martens,

D.P. Scott, V.J. Munster, E. de Wit, Clinical benefit of remdesivir in rhesus macaques infected with SARS-CoV-2, Nature 585 (7824) (2020) 273–276, https://doi.org/10.1038/s41586-020-2423-2325.
[43] M. Wang, R. Cao, L. Zhang, X. Yang, J. Liu, M. Xu, Z. Shi, Z. Hu, W. Zhong, G. Xiao, Remdesivir and chloroquine effectively inhibit the recently emerged novel coronavirus (2019-nCoV) in vitro, Cell Res. 30 (2020) 269–271, https://doi.org/10.1038/s41422-020-0282-0.
[44] L.C. Nguyen, D.M. Renner, D. Silva, D. Yang, N.A. Parenti, K.M. Medina, V. Nicolaescu, H. Gula, N. Drayman, A. Valdespino, A. Mohamed, C. Dann, K. Wannemo, L. Robinson-Mailman, A. Gonzalez, L. Stock, M. Cao, Z. Qiao, R. E. Moellering, S. Tay, G. Randall, M.F. Beers, M.R. Rosner, S.A. Oakes, S.R. Weiss, SARS-CoV-2 diverges from other betacoronaviruses in only partially activating the IRE1α/XBP1 endoplasmic reticulum stress pathway in human lung-derived cells, mBio 13 (2022) e0241522, https://doi.org/10.1128/mbio.02415-22.
[45] C.P. Chan, K.L. Siu, K.T. Chin, K.Y. Yuen, B. Zheng, D.Y. Jin, Modulation of the unfolded protein response by the severe acute respiratory syndrome coronavirus spike protein, J. Virol. 80 (2006) 9279–9287, https://doi.org/10.1128/JVI.00659-06.
[46] G.A. Versteeg, P.S. Van De Nes, P.J. Bredenbeek, W.J. Spaan, The coronavirus spike protein induces endoplasmic reticulum stress and upregulation of intracellular chemokine mRNA concentrations, J. Virol. 81 (2007) 10981–10990, https://doi.org/10.1128/JVI.01033-07.
[47] L. Echavarría-Consuegra, G.M. Cook, I. Busnadiego, C. Lefèvre, S. Keep, K. Brown, N. Doyle, G. Dowgier, K. Franaszek, N.A. Moore, S.G. Siddell, E. Bickerton, B. G. Hale, A.E. Firth, I. Brierley, N. Irigoyen, Manipulation of the unfolded protein response: a pharmacological strategy against coronavirus infection, PLoS Pathog. 17 (2021) e1009644, https://doi.org/10.1371/journal.ppat.1009644.
[48] D. Wang, B. Zhou, T.R. Keppel, M. Solano, J. Baudys, J. Goldstein, M.G. Finn, X. Fan, A.P. Chapman, J.L. Bundy, A.R. Woolfitt, S.H. Osman, J.L. Pirkle, D. E. Wentworth, J.R. Barr, N-glycosylation profiles of the SARS-CoV-2 spike D614G mutant and its ancestral protein characterized by advanced mass spectrometry, Sci. Rep. 11 (2021) 23561, https://doi.org/10.1038/s41598-021-02904-w.
[49] J.M. Oda, A.B. den Hartigh, S.M. Jackson, A.R. Tronco, S.L. Fink, The unfolded protein response components IRE1α and XBP1 promote human coronavirus infection, mBio 14 (2023) e0054023, https://doi.org/10.1128/mbio.00540-23.
[50] A. Köseler, R. Sabirli, T. Gören, I. Türkçüer, Ö. Kurt, Endoplasmic reticulum stress markers in SARS-COV-2 infection and pneumonia: case-control study, In Vivo 34 (3 Suppl) (2020) 1645–1650, https://doi.org/10.21873/invivo.11956.
[51] X. Ren, W. Wen, X. Fan, W. Hou, B. Su, P. Cai, J. Li, Y. Liu, F. Tang, F. Zhang, et al., COVID-19 immune features revealed by a large-scale single-cell transcriptome atlas, Cell 184 (2021), https://doi.org/10.1016/j.cell.2021.01.53, 1895-1913.e19.
[52] A. Choudhury, N.V. Das, R. Patra, S. Mukherjee, In silico analyses on the comparative sensing of SARS-CoV-2 mRNA by the intracellular TLRs of humans, J. Med. Virol. 93 (2021) 2476–2486, https://doi.org/10.1002/jmv.26776.
[53] M. Zheng, R. Karki, E.P. Williams, D. Yang, E. Fitzpatrick, P. Vogel, C.B. Jonsson, T. D. Kanneganti, TLR2 senses the SARS-CoV-2 envelope protein to produce inflammatory cytokines, Nat. Immunol. 22 (2021) 829–838, https://doi.org/10.1038/s41590-021-00937-x.
[54] R. Planès, J.B. Bert, S. Tairi, L. BenMohamed, E. Bahraoui, SARS-CoV-2 envelope (E) protein binds and activates TLR2 pathway: a novel molecular target for COVID-19 interventions, Viruses 14 (2022) 999, https://doi.org/10.3390/v14050999.
[55] R. Song, Y. Gao, I. Dozmorov, V. Malladi, I. Saha, M.M. McDaniel, S. Parameswaran, C. Liang, C. Arana, B. Zhang, IRF1 governs the differential interferon-stimulated gene responses in human monocytes and macrophages by regulating chromatin accessibility, Cell Rep. 34 (2021) 108891, https://doi.org/10.1016/j.celrep.2021.108891.
[56] P. Laurent, C. Yang, A.F. Rendeiro, B.E. Nilsson-Payant, L. Carrau, V. Chandar, Y. Bram, B. tenOever, O. Elemento, L.B. Ivashkiv, Sensing of SARS-CoV-2 by pDCs and their subsequent production of IFN-I contribute to macrophage-induced cytokine storm during COVID-19, Sci Immunol 7 (2022), https://doi.org/10.1126/sciimmunol.add4906 eadd4906.
[57] J.L. Fernandez, C. Mancebo, S. Garcinuño, G. March, Y. Alvarez, S. Alonso, L. Inglada, J. Blanco, A. Orduna, O. Montero, T.A. Sandoval, J.R. Cubillos-Ruiz, E. Bustamante, N. Fernandez, M. Sanchez Crespo, IRE1α-XBP1 activation elicited by viral singled stranded RNA via TLR8 may modulate lung cytokine induction in SARS-CoV-2 pneumonia, Genes Immun. (2023), https://doi.org/10.1038/s41435-023-00243-6.
[58] V. Salvi, H.O. Nguyen, F. Sozio, T. Schioppa, C. Gaudenzi, M. Laffranchi, P. Scapini, M. Passari, I. Barbazza, L. Tiberio, SARS-CoV-2–associated ssRNAs activate inflammation and immunity via TLR7/8, JCI Insight 6 (2021) e150542, https://doi.org/10.1172/jci.insight.
[59] G.R. Campbell, R.K. To, J. Hanna, S.A. Spector, SARS-CoV-2, SARS-CoV-1, and HIV-1 derived ssRNA sequences activate the NLRP3 inflammasome in human macrophages through a non-classical pathway, iScience 24 (2021) 102295, https://doi.org/10.1016/j.isci.2021.102295.
[60] M.A. Moreno-Eutimio, C. López-Macías, R. Pastelin-Palacios, Bioinformatic analysis and identification of single-stranded RNA sequences recognized by TLR7/8 in the SARS-CoV-2, SARS-CoV, and MERS-CoV genomes, Microbes Infect. 22 (2020) 226–229, https://doi.org/10.1016/j.micinf.2020.04.009.
[61] S. Márquez, J.J. Fernández, E. Terán-Cabanillas, C. Herrero, S. Alonso, A. Azogil, O. Montero, T. Iwawaki, J.R. Cubillos-Ruiz, N. Fernández, M. Sánchez Crespo, Endoplasmic reticulum stress sensor IRE1α enhances IL-23 expression by human dendritic cells, Front. Immunol. 8 (2017) 639, https://doi.org/10.3389/fimmu.2017.00639.
[62] O.O. Glebov, Low-dose fluvoxamine modulates endocytic trafficking of SARS-CoV-2 spike protein: a potential mechanism for anti-COVID-19 protection by antidepressants, Front. Pharmacol. 12 (2021) 787261, https://doi.org/10.3389/fphar.2021.787261.
[63] M. Zimniak, L. Kirschner, H. Hilpert, N. Geiger, O. Danov, H. Oberwinkler, M. Steinke, K. Sewald, J. Seibel, J. Bodem, The serotonin reuptake inhibitor fluoxetine inhibits SARS-CoV-2 in human lung tissue, Sci. Rep. 11 (2021) 5890, https://doi.org/10.1038/s41598-021-85049-0.
[64] Y. Takenaka, R. Tanaka, K. Kitabatake, K. Kuramochi, S. Aoki, M. Tsukimoto, Profiling differential effects of five selective serotonin reuptake inhibitors on TLRs-dependent and-independent IL-6 production in immune cells identifies fluoxetine as preferred anti-inflammatory drug candidate, Front. Pharmacol. 13 (2022) 874375, https://doi.org/10.3389/fphar.2022.874375.
[65] D.A. Rosen, S.M. Seki, A. Fernández-Castañeda, R.M. Beiter, J.D. Eccles, J. A. Woodfolk, A. Gaultier, Modulation of the sigma-1 receptor-IRE1 pathway is beneficial in preclinical models of inflammation and sepsis, Sci. Transl. Med. 11 (478) (2019) eaau5266, https://doi.org/10.1126/scitranslmed.aau5266.
[66] D. Péricat, S.A. Leon-Icaza, M. Sanchez Rico, C. Mühle, I. Zoicas, F. Schumacher, R. Planès, R. Mazars, G. Gros, A. Carpinteiro, K.A. Becker, J. Izopet, N. Strub-Wourgaft, P. Sjö, N. Neyrolles, B. Kleuser, F. Limosin, E. Gulbins, J. Kornhuber, E. Meunier, N. Hoertel, C. Cougoule, Antiviral and anti-inflammatory activities of fluoxetine in a SARS-CoV-2 infection mouse model, Int. J. Mol. Sci. 23 (2022) 13623, https://doi.org/10.3390/ijms232113623.
[67] T. Omi, H. Tanimukai, D. Kanayama, Y. Sakagami, S. Tagami, M. Okochi, T. Morihara, M. Sato, K. Yanagida, A. Kitasyoji, H. Hara, K. Imaizumi, T. Maurice, N. Chevallier, S. Marchal, M. Takeda, T. Kudo, Fluvoxamine alleviates ER stress via induction of Sigma-1 receptor, Cell Death Dis. 5 (2014) e1332, https://doi.org/10.1038/cddis.2014.301.
[68] L. Rosa-Fernandes, L.C. Lazari, J.M. da Silva, V. de Morais Gomes, R.R.G. Machado, A.F. dos Santos, D.B. Araujo, J.V.P. Coutinho, G.S. Arini, C.B. Angeli, SARS-CoV-2 activates ER stress and unfolded protein response, BioRxiv (2021) https://doi:10.1101/2021.06.21.449284.
[69] W. Kamel, M. Noerenberg, B. Cerikan, H. Chen, A.I. Järvelin, M. Kammoun, J. Y. Lee, N. Shuai, M. Garcia-Moreno, A. Andrejeva, M.J. Deery, N. Johnson, C. J. Neufeldt, M. Cortese, M.L. Knight, K.S. Lilley, J. Martinez, I. Davis, R. Bartenschlager, S. Mohammed, A. Castello, Global analysis of protein-RNA interactions in SARS-CoV-2-infected cells reveals key regulators of infection, Mol. Cell 81 (2021) 2851–2867.e7, https://doi.org/10.1016/j.molcel.2021.05.023.
[70] L.C. Nguyen, D. Yang, V. Nicolaescu, T.J. Best, H. Gula, D. Saxena, J.D. Gabbard, S. N. Chen, T. Ohtsuki, J.B. Friesen, Cannabidiol inhibits SARS-CoV-2 replication through induction of the host ER stress and innate immune responses, Sci. Adv. (2022) eabi6110, https://doi.org/10.1126/sciadv.abi6110.
[71] D. Awasthi, S. Chopra, B.A. Cho, A. Emmanuelli, T.A. Sandoval, S.M. Hwang, C. S. Chae, C. Salvagno, C. Tan, L. Vasquez-Urbina, J.J. Fernandez Rodriguez, S. F. Santagostino, T. Iwawaki, E.A. Romero-Sandoval, M. Sanchez Crespo, D. K. Morales, I.D. Iliev, T.M. Hohl, J.R. Cubillos-Ruiz, Inflammatory ER stress responses dictate the immunopathogenic progression of systemic candidiasis, J. Clin. Invest. 133 (17) (2023) e167359, https://doi.org/10.1172/JCI167359.